5-2010

Analysis of Fresh Water Resources at the Line Hole Well Field, San Salvador Island, the Bahamas

Scot Allan Russell Jr.
Western Kentucky University, scot.russell277@wku.edu

ANALYSIS OF FRESH WATER RESOURCES AT THE LINE HOLE WELL FIELD, SAN SALVADOR ISLAND, THE BAHAMAS

A Thesis
Presented to
The Faculty of the Department of Geography and Geology
Western Kentucky University
Bowling Green, Kentucky

In Partial Fulfillment
Of the Requirements for the Degree
Master of Science in Geosciences

By
Scot Allan Russell Jr.

May 2010

ANALAYSIS OF FRESH WATER RESOURCES AT THE LINE HOLE WELL FIELD, SAN SALVADOR ISLAND, THE BAHAMAS

Date Recommended 4/23/2010

Dr. Lee Florea
Director of Thesis

Dr. Fred Siewers

Dr. Michael May

Dr. John Mylroie

Dean, Graduate Studies and Research Date

Table of Contents

List of Illustrations

ANALYSIS OF FRESH WATER RESOURCES AT THE LINE HOLE WELL FIELD, SAN SALVADOR ISLAND, THE BAHAMAS

Scot A. Russell Jr. May 2010 53 Pages

Directed by: Lee Florea, Michael May, Fred Siewers and John Mylroie

Department of Geography and Geology Western Kentucky University

A major economic constraint in the Bahamas, and other small carbonates islands world-wide, is the lack of fresh water resources. To combat these socio-economic problems on San Salvador Island I sought to gain a more detailed understanding of the extent, behavior, and controls on the island's fresh-water lens. DC electrical resistivity tomography and time-series geochemical data are used to study the fresh water lens at the Line Hole well field. Electrical Resistivity profiles are used to image the extent of fresh water resources. Time-series geochemical data provide information on the behavior of the fresh water resources as a function of time.

The inversion models of the electrical resistivity profiles illustrate a fresh water lens less than 3 meters thick on average. The mixing zone is diffuse in nature, and substantially thicker than the fresh water lens. The geochemical results corroborate the fresh water lens dimensions predicted by the electrical resistivity model. In addition, mixed semi-diurnal and spring/neap tidal cycles are the primary control on the water level. Statistical analysis of specific conductance and temperature illustrate a positive and negative correlation with water level, respectively. Analysis of precipitation with

respect to water level and geochemistry indicate low effective recharge rates during the period of study.

The current state of the water resources at the Line Hole well field is strained. Despite moderate levels of freshening since the termination of pumping in December 2006; the system continues to be in a state of disequilibrium. The problem is compounded by abnormal thickening of the mixing zone due to communication of the well field with the ocean, and a limited volume of fresh water. In conclusion, the two techniques used in conjunction provide a non-invasive method of estimating fresh water resources in this type of setting. Conversely, the high RMS and L2 values for the electrical resistivity models and limited time-series data create a high level of uncertainty in the interpretation of results.

1. Introduction

San Salvador Island is a small "out island" or "family island", which is defined as an island with a small rural population in the nation's periphery outside of Nassau (Sealey, 1990). The development of the Club Med resort in 1992 (Gamble et al., 2000), supported by the Bahamian government as a means of increasing the economic well being of San Salvador, has increased the rate of fresh water withdrawal from the Cockburn Town aquifer (Erdman et al., 1997). Since 1992 significant increases in pumping rates, and salinity of the water wells have been observed and positively correlated to Club Med's water usage (Erdman et al., 1997).

These water resource problems have two major effects on the island's infrastructure. The first of these problems is addressed by Cant (1996), who reported that one of the major obstacles of economic development in the Bahamas and other small carbonate islands is the limited supply of fresh water. Second, the quality of life on the island is a function of the availability of fresh water. The increase in mean salinity in the water supply may have detrimental health effects on the local population such as sodium hypertension (Erdman et al., 1997).

To aid in the fight against these socio-economic problems I sought to gain a more detailed understanding of the extent, behavior, and controls on San Salvador Island's fresh-water lens. This hydrogeological case study of the Line Hole well field uses a combination geochemical-geophysical approach to study fresh water resources in this dynamic aquifer.

2. Field Site

San Salvador Island is an approximately 150 km^2 island located on an isolated carbonate platform, 310km southeast of New Providence and 640 km east southeast of Florida in the eastern section of the Bahamian archipelago (Figure 2.1). The island is composed of arc-shaped ridges with elevations that exceed 30 meters. The majority of lakes on San Salvador Island form in the depressions between these ridges. These landlocked lakes and associated wetlands account for approximately forty percent of the total area of the island (Roebuck et al., 2004). Like most Bahamian islands there is no fresh surface water, and any hydrologic connection between the ocean and the island is in the form of preferred pathways and phreatic conduits (Davis and Johnson, 1989).

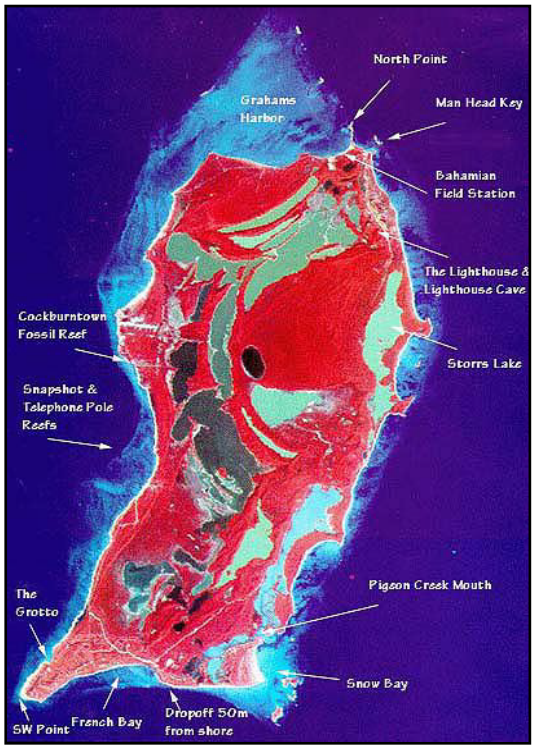

Figure 2.1: Infrared map of San Salvador Island adapted from. Three lake colorations are present in the map: the light blue lakes are hypersaline; the green lakes have an intermediate salinity and high cyanobacteria productivity; and the dark lakes have a marine salnity. Map was adapted from Dr. Kari Benson's website: http://benson-k.web.lynchburg.edu/bahamas/sansal.html

2.1. Quaternary Sea Level and Stratigraphy

The majority of the geologic description of San Salvador Island is drawn from the "Field Guide to Geology and Karst Hydrogeology of San Salvador Island" by Mylroie and Carew (2008). The exposed rock record of San Salvador Island is solely late Pleistocene and Holocene carbonates (Meyerhoff and Hatten, 1974). The primary driving force behind changes in sedimentation in the Bahamas is glacio-eustatic sea level fluctuations. The waxing and waning of ice sheets drives global sea level fall and rise, respectively.

The Bahamas have been at a sea level low stand for approximately 85 to 90 percent of the Quaternary. Primary deposition in the Bahamas occurs during the short period of time that the islands were experiencing a sea-level high stand. During sea level high stands individual carbonate packages are deposited and separated by erosional unconformities and terra rossa paleosols formed during the subsequent lowstands. There are three phases of each depositional package: transgressive-phase, still-stand phase, and regressive-phase. Each of these phases has a subtidal, intertidal, and eolianite component.

The initiation of the depositional packages begins with a marine transgression. These transgressing waters flood the platform, and wave action mobilizes the carbonate sediment to form large dunes. As the transgression continues, all but the most pronounced dune ridges are destroyed. Following the transgressive phase, the still-stand phase is dominated by the building up of coral reefs to wave base. During this still-stand phase eolianite production begins to decrease as a result of the coral reef development

lowering wave energy, and effectively halts the supply of sediment. Following the still-stand phase, a sea-level regression causes eolianites to be deposited until the sea level reaches the lower limit of the platform. The final step in this sequence is a sea level low stand which exposes rocks to weathering processes. This low-stand phase is typically associated with an erosional unconformity and the development of terra rossa paleosols.

2.2. Distribution of Fresh Water

The climate of San Salvador has been classified as the Köeppen Aw (Tropical Savannah) climate type, which is characterized by dry winters and constant temperatures (Shaklee, 1996). Over-pumping of water wells on this relatively dry island has become a major issue with the opening of a Club Med resort on the island. Declines in tourism-related revenue, the costs of importing water, and the building of a reverse osmosis desalinization plant are some of the major financial strains on San Salvador Island due to saltwater intrusion.

San Salvador Island has a rate of evapotranspiration ranging from 1,250 to 1,375 mm/yr (Sealey, 1994), and precipitation rates ranging from 500 to 2,000 mm/yr. With no surface water component, the mean annual water budget for the island is solely dependent on this balance between precipitation and evapotranspiration (Crump, and Gamble, 2006). This negative water budget in conjunction with the presence of interdune impressions creates hypersaline lakes. These inter-dune lakes draw up the potentiometric surface and divide the fresh ground water into small, isolated fresh water lenses under the

dune ridges. Results by Schneider and Kruse (2005) establish that when anthropogenic influences are included in the water budget the fresh water lens is depleted even further.

Geologically, Whitaker and Smart (2004) have identified two carbonate aquifers, with very different permeability characteristics, that are used for water supply in the Bahamas and the Turks and Caicos Islands. The first aquifer studied consisted of local strand and beach sands from the unconsolidated to partially consolidated Holocene aquifer of the Rice Bay Formation (San Salvador Island), which is characterized by high primary porosity and relatively low hydraulic conductivity (Whitaker and Smart, 2004). Conversely, the principle aquifer on most islands is the Pleistocene Lucayan Limestone, which includes the Owl's Hole and Grotto Beach (San Salvador Island) Formations, which has high hydraulic conductivities due to the development of dissolutionally enhanced permeability (Vacher, 1988; Whitaker and Smart, 2004). DGH analyses by Vacher (1988) also suggest that the fresh water lens will be thicker in the Holocene Rice Bay Formation where permeability is lower.

2.3. Line Hole Well Field

The Line Hole well field includes 12 water wells used by the United Estates settlement, on the north-central shore of the island, from the mid 1990's to December, 2006. Termination of pumping in this well field in December of 2006 was direct

related to pumping-induced salt water intrusion. It has been documented by Gaughan and Davis (2009) that since the pumping was terminated the wells have begun to freshen again.

The history of the Line Hole well field provides a case example for studying the occurrence of fresh water in an area that has experienced salt-water intrusion. Shorter than expected tidal lag times in the well field observed by Gaughan and Davis (2009) is used to support the presence of phreatic conduits below the well field. This theory is also supported by large dissolutional features (banana holes) several meters away from the North 5 water well. Although these banana holes cannot be directly used as evidence of conduit flow; they do illustrate dissolutional effects of the fresh-water lens in the well field.

.

3. Ghyben-Herzberg Principle

Fresh water resources in carbonate islands with relatively small catchment areas occur in lens of fresh water which buoyantly overlay saline groundwater (Mylroie, Carew, and Vacher, 1995). The size and shape of these fresh-water lenses are expressed by the Ghyben-Herzberg (GH) theory (Ghyben, 1988; Herzberg, 1901). The Ghyben-Herzberg Principle in its simplest form states that at equilibrium, the elevation of the potentiometric surface and depth of the fresh water/salt water interface are related by the following equation

$$z = \alpha h \text{ and } \alpha = (\rho_f)/(\rho_s - \rho_f) \quad [1]$$

where h is elevation of the potentiometric surface above sea level, z is the depth of the fresh water/salt water interface below sea level, α is the density difference ratio, and ρ_f and ρ_s are the densities of fresh and the underlying saline ground water, respectively. Using the normal densities for fresh (1.000 g.cm3) and saline (1.025 g/cm3) ground water, the constant of proportionality between z and h is approximately 40.

The following description of the effects of aquifer heterogeneity, and differential recharge on fresh-water lens morphology is drawn primarily from Vacher (1988). The traditional Ghyben-Herzberg fresh-water lens occurs on islands with small catchments, relatively high permeabilities, and/or low recharge rates. Although the principles behind the GH theory are simple, a wide range of lens geometries can result from differences in the spatial distribution of hydraulic conductivity and recharge. The Dupuit-Ghyben-

Herzberg analyses by Vacher (1988) have quantified the effects of aquifer heterogeneity and anisotropy on the distribution of fresh water. Lithologies with high porosity and low permeability create a thick fresh water lens. More permeable units provide less resistance to flow, and therefore can thin or truncate the fresh-water lens. The sedimentary architecture of an island is therefore germane to the distribution of freshwater.

In terms of effective recharge, the DGH models created by Vacher in 1988 (Figure 3.1) illustrate a positive correlation between Recharge, and lens thickness. Conversely, tidal forcing, and over-pumping of water wells creates significant disturbances to the prototypical DGH fresh water lens.

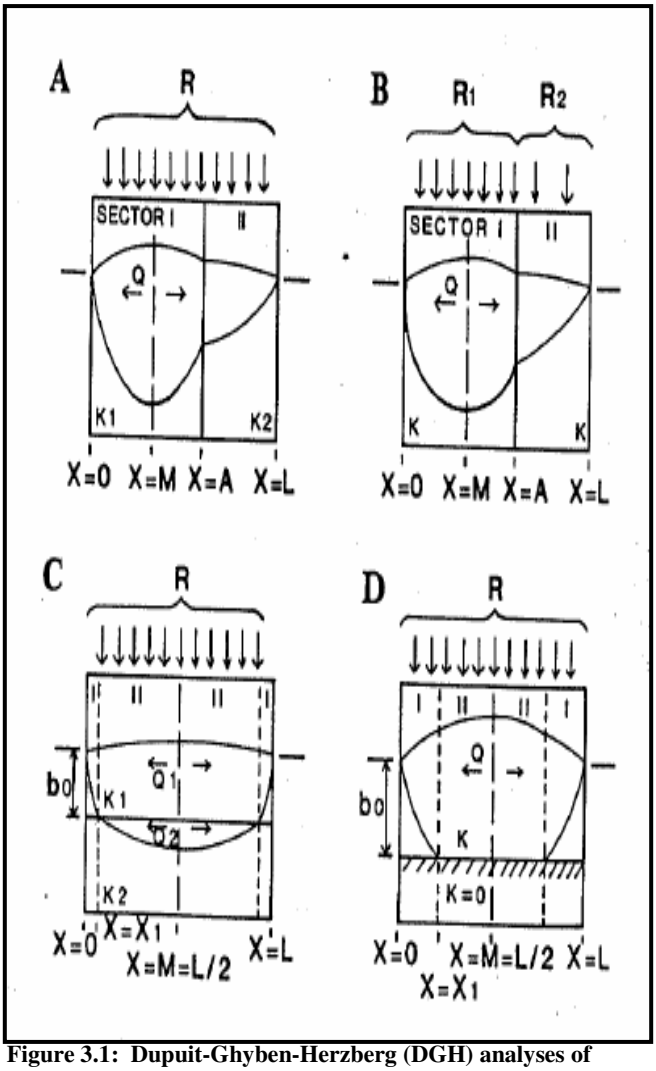

Figure 3.1: Dupuit-Ghyben-Herzberg (DGH) analyses of fresh-water lenses experiencing differential recharge and lithological heterogeneity. Diagram A is an illustration of the effects of two different hydraulic conductivities with a vertical boundary on fresh-water lens morphology with constant recharge. Diagram B is an illustration of the effects of two different hydraulic conductivities, and differential recharge on fresh water lens morphology. Diagram C is an illustration of the effects of two different hydraulic conductivities with a horizontal boundary on fresh-water lens morphology with constant recharge. Diagram D is an illustration of the effects of an impermeable layer on fresh-water lens morpholohy with constant recharge. This figure was adapted from Vacher (1988).

Tidal variations create changes in the hydraulic head gradient which promotes mixing of fresh and saline ground water. More directly, Davis and Johnson (1989) postulated that sea water is introduced into the aquifers due to tidal forcing through phreatic conduits.

The limited fresh water resources on an island are also severely stressed due to over pumping of water wells. The process allows for drawdown of the potentiometric surface, and up-coning of saline ground water. In extreme cases this process can cause a complete fragmentation of the fresh-water lens into smaller constituents.

4. Electrical Resistivity Theory

The majority of the following information on electrical resistivity theory was largely adopted from Lowrie (2007). The basic theory of the electrical resistivity method is that a measurable current can be introduced by an electrode at the surface in a uniform half space. The equipotential lines of the electrical field are hemispherical and current flows away from the electrode and normal to the equipotential lines (Figure 4.1). The equipotential surfaces for a sink electrode are also hemispherical, but the electrical field lines converge towards the electrode parallel to the current flow.

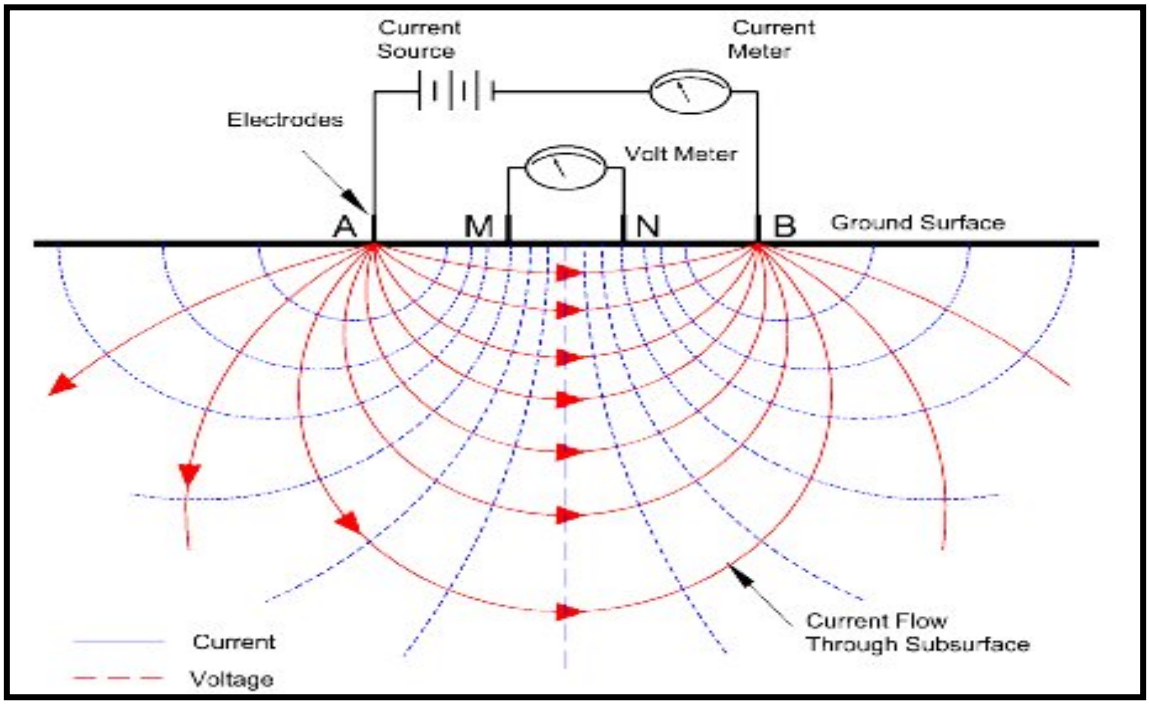

Figure 4.1: Diagram of the four-electrode array that is the basis behind the electrical resistivity method. Electrodes A and B are the current electrodes, and electrodes M and N are the potential electrodes. A current is induced into the subsurface via current electrode A and travels in the the subsurface (red solid lines) normal to the equipotential lines (blue dotted lines) to current electrode B. Voltage is measured at electrodes M and N; and the potential difference (ΔV) is calculated. This figure is adapted from the Nowrthwest Geophysicsal Associates Inc. website: http://www.nga.com/Geo_ser_DC_tech.htm.

4.1. Ohm's Law

In its most elementary form, electrical resistivity theory is based upon the theory derived by the German scientist Georg Simon Ohm. In 1827, Ohm postulated that the electric current I in a conducting wire is proportional to the potential difference ΔV across it. This linear relationship is expressed by the equation:

$$I = \frac{V}{R} \quad [2]$$

where R is the resistance of the wire in units of ohms (Ω).

A more precise configuration of Ohm's Law states that for a given material the resistance is proportional to the configuration of the electrode set-up which is expressed as the geometric factor k. These relationships are expressed by the equation

$$\rho = \frac{R}{k} \quad [3]$$

where ρ is the resistivity of the conductor in ohm-meters (Ω m). The combination of the preceding equation with the basic form of Ohm's Law yields a relationship expressed by the following equation

$$E = \rho J \quad [4]$$

where E is the magnitude of the electrical field and J is the magnitude of the current density.

4.2. Archie's Law of Earth Conductance

The electrical resistivity method is used to detect signals induced in subsurface conducting bodies by an electric field generated above ground. The important physical property of rocks for this method is the resistivity (Ω m). In the general form Archie's Law states that the resistivity of a rock is strongly influenced by the presence of ground water, which acts as an electrolyte. The minerals that form the matrix of a rock are generally poorer conductors than groundwater, so the resistivity of the medium increases with increasing water saturation. The resistivity of the rock is proportional to the resistivity of the ground water, which is quite variable because it depends on the concentration and type of dissolved minerals and salts it contains. In coastal aquifers ground water saturating the rock can range from fresh to saline. A rock containing saline ground water will yield a lower resistivity measurement due to the added electrolytes.

4.3. Electrical Resistivity Arrays

Measurements of electrical resistivity in the earth are based on the general four electrode method. This method requires a pair of current electrodes, and a pair of

potential electrodes. The current electrodes A and B act as source and sink, respectively. At the detection electrode M the potential due to the source A is $+\rho I/(2\pi r_{AM})$, while at the detection electrode N the potential due to the sink B is $-\rho I/(2\pi r_{MB})$. The combined potential at M is

$$U_M = \frac{\rho I}{2\pi\left(\frac{1}{r_{AM}} - \frac{1}{r_{MB}}\right)} \quad [5]$$

Similarly, the resultant potential at N is

$$U_N = \frac{\rho I}{2\pi\left(\frac{1}{r_{AN}} - \frac{1}{r_{NB}}\right)} \quad [6]$$

The potential difference measured by a voltmeter connected between M and N is

$$V = \frac{\rho I}{2\pi\left[\left(\frac{1}{r_{AM}} - \frac{1}{r_{MB}}\right) - \left(\frac{1}{r_{AN}} - \frac{1}{r_{NB}}\right)\right]} \quad [7]$$

All quantities in this equation can be measured at the ground surface except the resistivity, which is given by

$$\rho = 2\pi\frac{V}{I}\left[\left(\frac{1}{r_{AM}} - \frac{1}{r_{MB}}\right) - \left(\frac{1}{r_{AN}} - \frac{1}{r_{NB}}\right)\right]^{-1} \quad [8]$$

The most commonly used configurations are the Wenner, Schlumberger, and dipole-dipole arrangements (Figure 4.3.1).

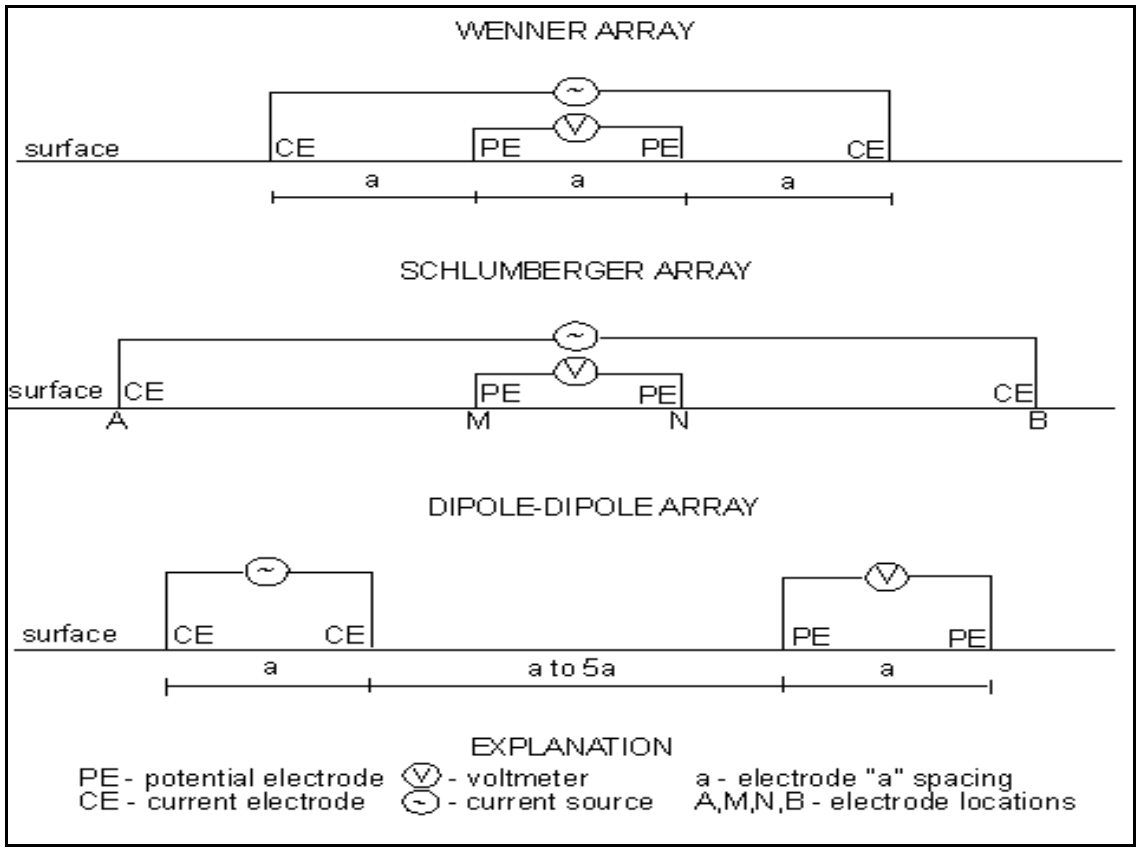

Figure 4.3.1: Diagram of the three most common electrical resistivity arrays adapted from the New Jersey Geological Survey website: http://www.state.nj.us/dep/njgs/geophys/elec.htm.

In the Wenner configuration the current and potential electrode pairs have a common mid-point and the distances between adjacent electrodes are equal, so the $r_{AM} = r_{NB} = a$, and $r_{MB} = r_{AN} = 2a$. The substitution of these values into Eq. (8) yields

$$\rho = 2\pi a \frac{V}{I} \quad [9]$$

According to Coggon (1973), Dey et al. (1975), and Van Zijl, (1985) the Werner array has a high signal response, and is effective at resolving horizontal structures. Conversely, it creates a high level of electromagnetic coupling noise, and has a low sensitivity to surface inhomogeneities with respect to profiling.

In the Schlumberger configuration the current and potential pairs of electrodes often also have a common mid-point, but the distances between adjacent electrodes differ. Let the separations of the current and potential electrodes be L and a, respectively. Then $r_{AM} = r_{NB} = (L-a)/2$ and $r_{AN} = r_{MB} = (L+a)/2$. The substitution of these values into Eq. 8 yields

$$\rho = \frac{\pi V}{4 I}\left(\frac{L^2 - a^2}{a}\right) \quad [10]$$

In this configuration the separation of the current electrodes is kept much larger than that of the potential electrodes (L >> a). Under these conditions Eq. (10) simplifies to

$$\rho = \frac{\pi V}{4 I}\left(\frac{L^2}{a}\right) \quad [11]$$

According to Coggon (1973), Dey et al. (1975), and Van Zijl, (1985) the Schlumberger array is also effective at resolving horizontal structures, but is slightly better at vertical profiling than the Wenner array. The Schlumberger has a higher sensitivity to surface inhomogeneities when sounding than any other electrode array discussed. The

disadvantages of this method are its sensitivity to surface inhomogeneities with respect to profiling, and its high level of electromagnetic coupling noise.

In the dipole-dipole configuration the spacing of the electrodes in each pair is a, while the distance between their mid-points is L, which is generally much larger than a. Note that detection electrode D is defined as the potential electrode closer to current sink B. In this case $r_{AN} = r_{BM} = L$, $r_{AM} = L + a$, and $r_{BN} = L - a$. The substitution of these values into Eq. (8) yields

$$\rho = \pi \frac{V}{I}\left(\frac{L(L^2 - a^2)}{a^2}\right) \quad [12]$$

According to Coggon (1973), Dey et al. (1975), and Van Zijl, (1985) the dipole-dipole array is effective at resolving horizontal structures, has low electromagnetic coupling noise, and is the most effective array at detecting surface heterogeneities with respect to profiling. Conversely, the dipole-dipole array is relatively ineffective at vertical profiling.

Temporal and logistical constraints during field work allowed for the use of one array configuration. The dipole-dipole array was chosen because of its effectiveness at profiling, and its low electromagnetic coupling noise. The target for this study is the fresh water/salt water interface which will be manifested as a shallow, spatially extensive low resistivity anomaly. Profiling is therefore much more effective at capturing this feature. The subsurface of carbonate islands is dominated by saturated carbonate rocks which have a high conductivity. This highly conductive medium creates a lot of noise, and it is believed that the dipole-dipole array minimizes noise.

4.4. Electrical Resistivity Inversion

In the idealized case of a perfectly heterogeneous, isotropic, conducting half-space the resistivity determined with a four-electrode configuration is the true resistivity of the half space. Conversely, in reality the subsurface is heterogeneous and anisotropic due to lithological variation and geological structures. The actual results from these measurements are the apparent resistivity which generally does not represent the true resistivity of any part of the ground.

Electrical Resistivity Tomography (ERT) is a method of converting an apparent resistivity distribution to a model of the true resistivity of the subsurface to depths of several tens of meters. In electrical resistivity tomography, an inversion procedure is applied to the electrical potentials measured between electrode pairs to obtain the resistivity structure along the current flow lines. An inversion model is used to calculate model parameters from observed data as opposed to a forward model where the observed data is calculated from a model. In terms of this method, the data is acquired, and the field and then iterative statistical calculations are used to create a model of subsurface resistivity distribution beneath the electrode array.

5. Methodology

Figure 5.1: Diagramatic map of the Line Hole well field with the location of data collection sites illustrated. The short red line is the beach electrical resistivity transect, and the long red line is the long electrical resistivity transect. The short black line overlying the long transect is the ridge electrical resistivity transect. The black circles are, from north to south, the N5, N4, N3, N2, S1, S2, S3, S4, S5, and SWA water wells. The pink circles are, from north to south, the NA, N1, and SEA water wells. The pink circles indicate data collection wells. The Black square in the middle of the well field is the pump house.

Time-series data of geochemical parameters and water-level were collected in the north abandoned water well at the Line Hole well field on San Salvador Island, Bahamas. Two YSI multi-parameter geochemical datasondes were programmed to collect measurements from January 3, 2009 to February 19, 2009 at ten minute intervals. The following geochemical parameters were measured by the datasondes: pH, specific conductance, dissolved oxygen, and temperature. The datasondes were installed at 7 meters, and 11 meters below the top of the casing for the north abandoned water well (Figure 5.1). Time-series water level data was collected using (2) CS pressure transducer connected to Campbell Scientific CR10X data loggers, and (1) YSI pressure transducer from January 3, 2009 to June 29, 2009. The two CS pressure transducers were installed

in the north 1 and southeast abandoned water wells at a depth of 5 meters below the top of the well casing, and the YSI pressure transducer was installed in the north abandoned water well at a depth of 10 meters below the top of the well casing (Figure 5.1). A HOBO Onset rainfall gauge was installed at the pumping station in the center of the well field. The period of data collection for the rainfall gauge is identical to the pressure transducers. The time-series data collected from the Line Hole well field were analyzed statistically using MATLAB, and Microsoft Excel. Scatter plots, and correlograms of the time-series data were created to identify trends in the data.

In addition to the time-series data, DC Electrical Resistivity Tomography (ERT) transects were also collected during the period of June 29, 2009 and July 2, 2009. The equipment used for the collection of this data is the AGI Sting R1 Earth Resistivity Meter, and the AGI Earth Imager 2D software package was used to create two-dimensional inversion models of the raw data. The array type used ws the dipole-dipole array with an electrode spacing of 2.8 meters, 2.8 meters, and 6.27 meters respectively. A total of three ERT transects were collected (Figure 5.1): the first transect begins at the high tide line (-74.4866°, 21.1164°) and extends 75.6 meters inland to the north edge of the road (-74.4870°, 21.1158°), the second transect begins at the south edge of the road (-74.4861°, 24.1184°) and extends 75.6 meters across the Pleistocene dune-ridge (-74.4899°, 24.1148°), and the third transect begins at the south edge of the road (-74.4861°, 24.1184°) and extends 168 meters inland across the Pleistocene dune ridge (-74.4889°, 24.1130°).

Using Earth Imager 2D, the following three cross-sections were generated for each ERT transect: measured apparent resistivity pseudo-section, inverted resistivity

section, and calculated apparent resistivity pseudo-section. The measured apparent resistivity pseudo-section is a display of the field measurements of apparent resistivity. The inverted resistivity section is the model of the subsurface resistivity distribution based upon the measured apparent resistivities. The calculated apparent resistivity pseudo-section is a calculation of the apparent resistivity measurements based upon the predicted resistivity distribution. This last cross-section is used as a visual measure of the accuracy of the model.

6. Geochemical Results

The graph of water level and precipitation with respect to time (Figure 6.1) reveals no correlation between water level and rainfall events. The graphs of specific conductance (Figure 11.1), pH (Figure 11.2), dissolved oxygen (Figure 11.3) , and temperature (Figure 11.4) with respect to temperature also illustrate this lack of a relationship. Autocorrelation plots of the same variables (Figures 11.5) confirm these observations due the lack of maximum autocorrelations corresponding to the timing of precipitation events.

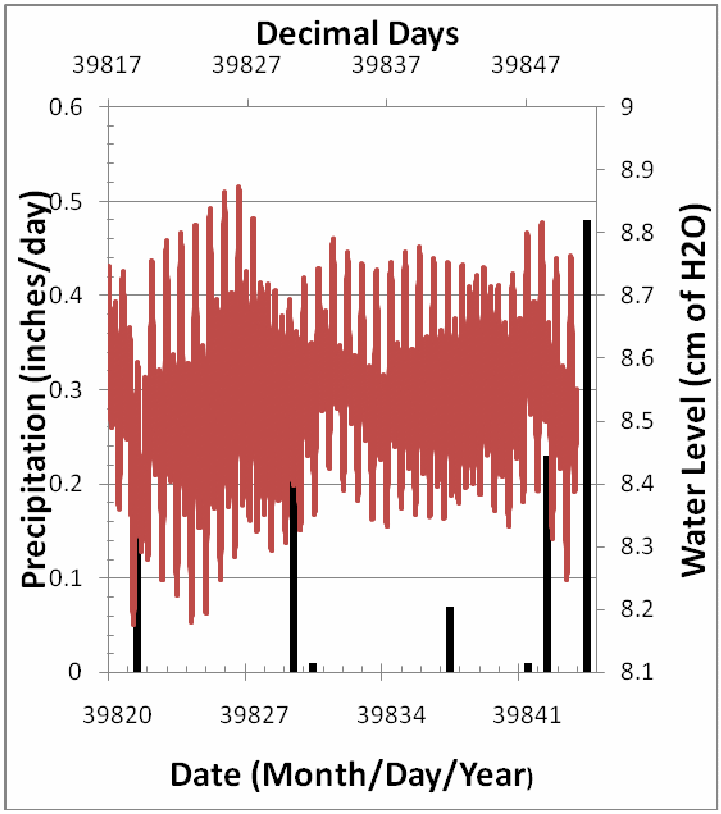

Figure 6.1: Time-series graph of precipitation and water level with respect to time. On the primary y-axis is precipitation (black) measured in inches per day, and on the primary x-axis is the date of rainfall events. On the secondary y-axis is water level measured at a depth of 10 meters, and on the secondary x-axis is time measured in decimal days.

Two significant temporal trends are observed in the graph of water level with respect to time (Figure 6.1). The first trend is a mixed semi-diurnal cycle with the larger of the two peaks occurring in the morning. The autocorrelation function of water level at 100 lags (Figure 6.2) confirms this trend. The maximum positive autocorrelation occurs at 0 lags and the maximum negative autocorrelation occurs at approximately 26 lags

(4.33 hours). The second trend is also cyclic, but has a wavelength of approximately 20 days. The autocorrelation function of water level at 4000 lags (Figure 6.3) confirms this trend. The primary maximum positive autocorrelation occurs at 0 lags, and the secondary maximum positive autocorrelation occurs at approximately 2,100 lags (14.58 days).

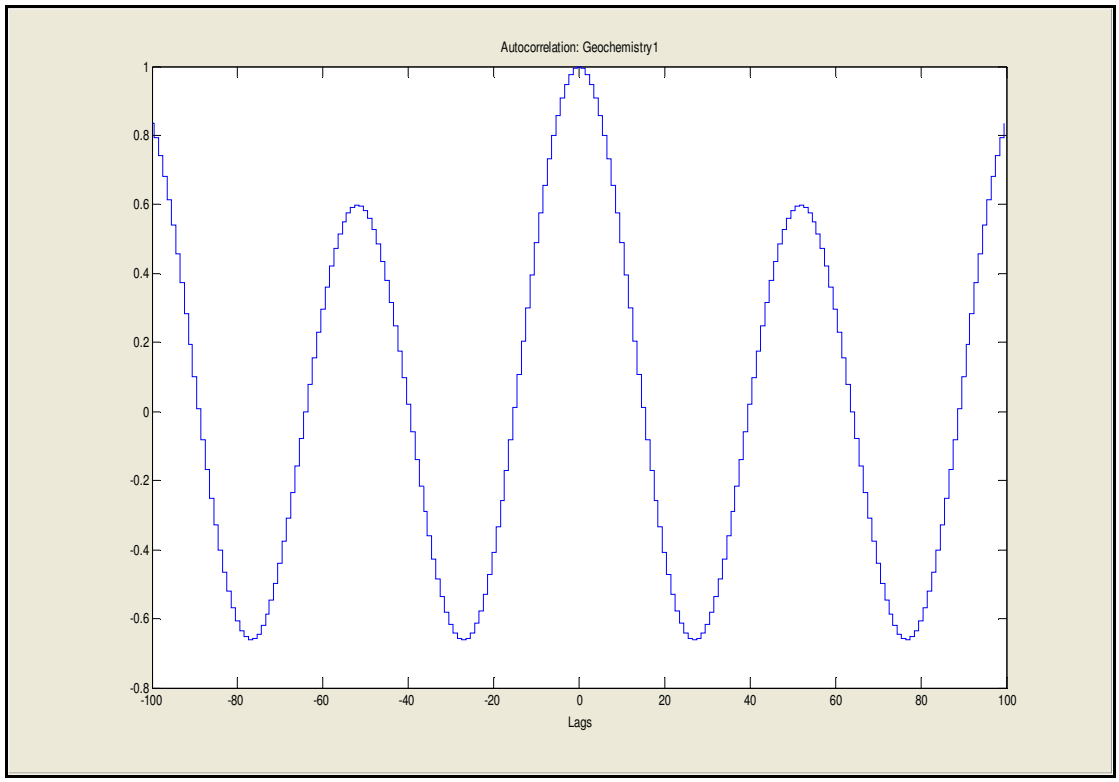

Figure 6.2: Graph of the autocorrelation function of water level data collected at 10 meters depths in the North Abandoned Well with 4000 lags. On the x-axis is time in terms of lags (1 lag is equivalent to 10 minutes), and on the y-axis is the degree of autocorrelation.

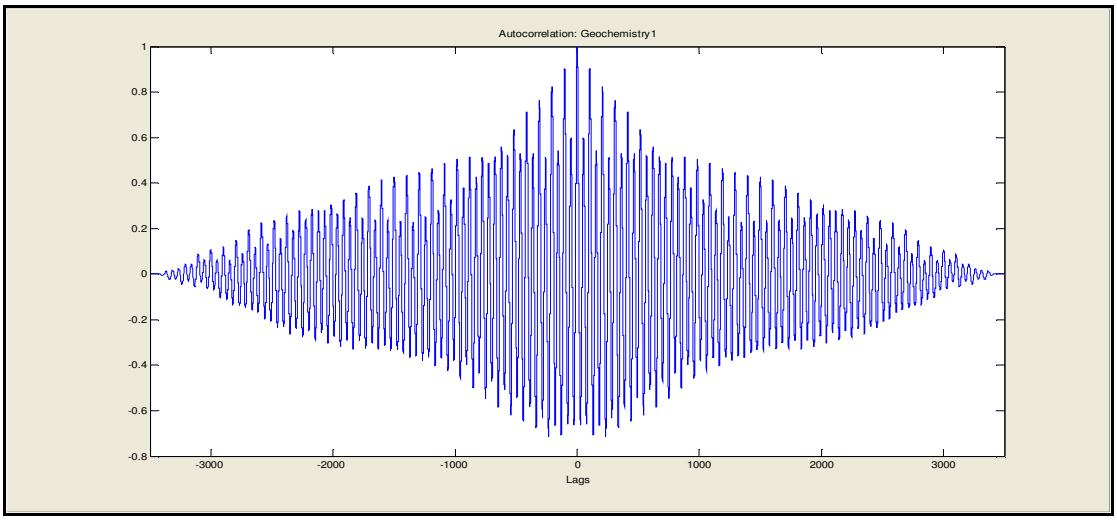

Figure 6.3: Graph of the autocorrelation function of water level data collected at 10 meters depths in the North Abandoned Well with 100 lags. On the x-axis is time in terms of lags (1 lag is equivalent to 10 minutes), and on the y-axis is the degree of autocorrelation.

The graph of specific conductance with respect to time (Figure 6.4) illustrates a mixed semi-diurnal signal at both 7 and 11 meters depth. With respect to depth, average specific conductance increases from 1064 μS/cm at 7 meters to 10,881 μS/cm at 11 meters (Figure 6.4). There is a small amount of lag time in between the water level maxima, and the specific conductance maxima. The cross-correlation function of specific conductance with respect to water level at 100 lags is used to confirm this trend and to quantify the lag (Figure 6.5). The maximum positive correlation between specific conductance and water level occurs at 8 lags (1.33 hours) and reaches maximum negative correlation at approximately 35 lags (5.83 hours).

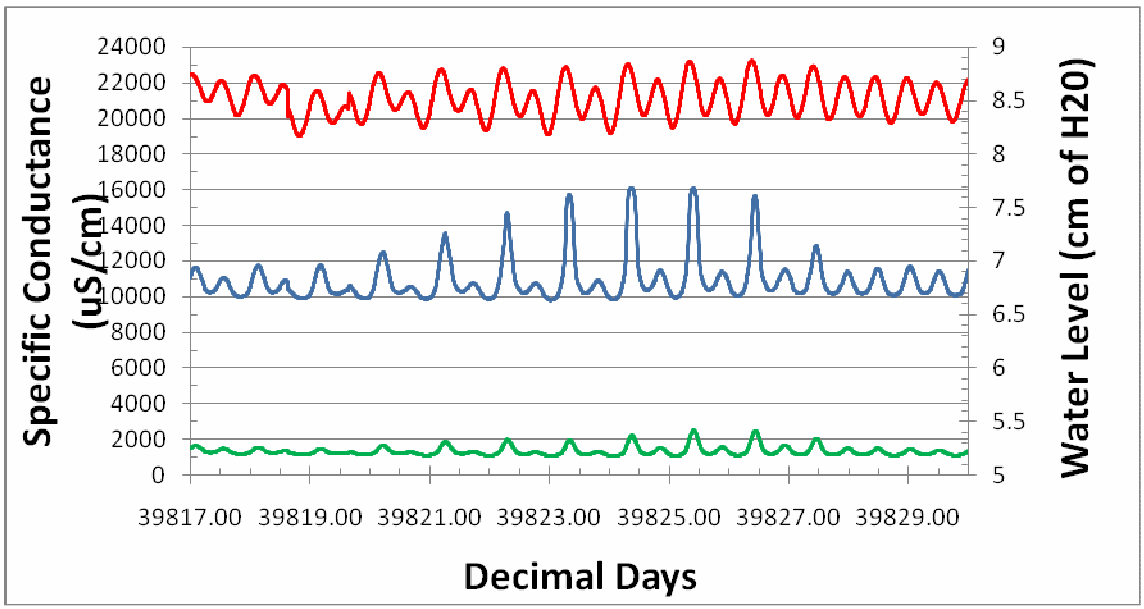

Figure 6.4: Specific conductance in µS/cm, at depths of seven (green) and eleven (blue) meters are plotted on the primary vertical axis (left-hand axis) with respect to time in decimal days. Water level data in cm of water (red) are plotted on the secondary vertical axis (right-hand axis) with respect to time.

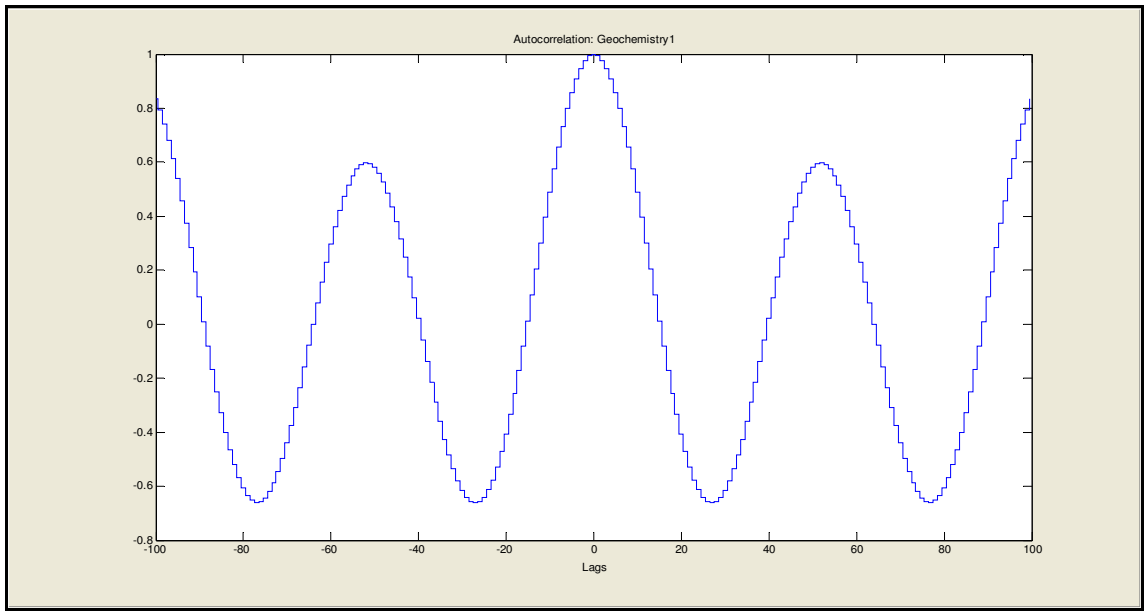

Figure 6.5: Graph of the cross-correlation function of specific conductance data collected at 11 meters depth with respect to water level in the North Abandoned Well with 100 lags. On the x-axis is time in terms of lags (1 lag is equivalent to 10 minutes), and on the y-axis is the degree of cross-correlation.

The graph of temperature with respect to time (Figure 6.6) illustrates a mixed semi-diurnal signal at both 7 and 11 meters depth. Conversely, the temporal trend in temperature is anti-correlated with water level. With respect to depth, average temperature increases from 26.4 °C at 7 meters to 26.8 °C at 11 meters (Figure 6.6). There is a small amount of lag time in between the water level maxima, and the temperature maxima. The cross-correlation function of temperature with respect to water level at 100 lags is used to quantify this lag (Figure 6.7). The maximum positive correlation between temperature and water level occurs at 3 lags (0.50 hours) and reaches maximum negative correlation at approximately 30 lags (5.00 hours).

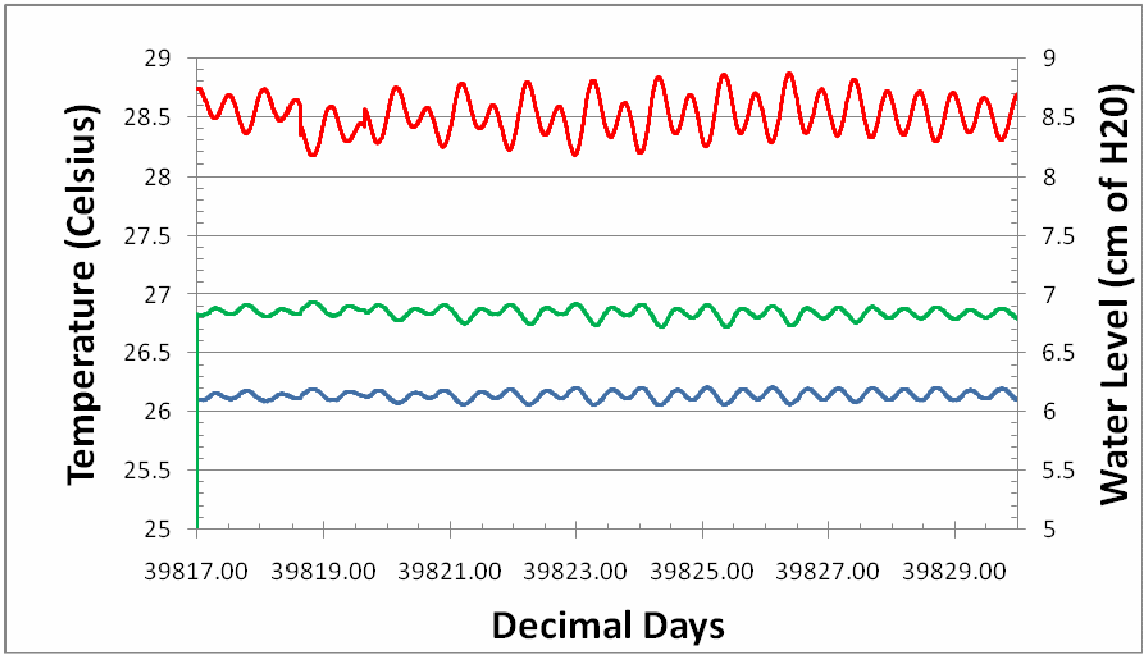

Figure 6.6: Temperature at depths of seven (green) and eleven (blue) meters are plotted on the primary vertical axis (left) with respect to time in decimal days. Water level data in cm of water (red) are plotted on the secondary vertical axis (right) with respect to time.

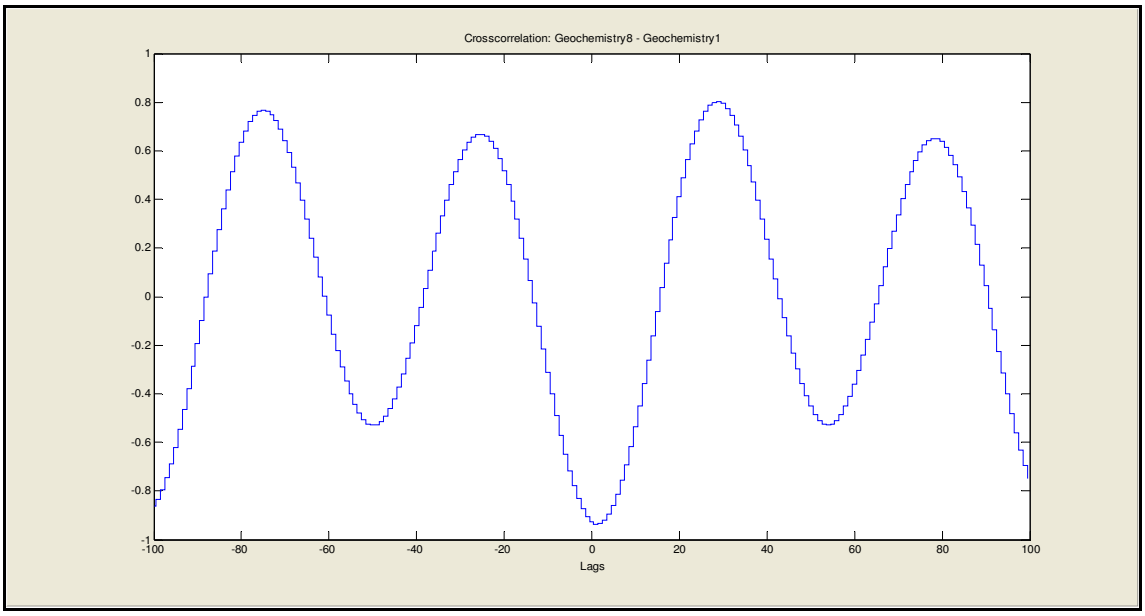

Figure 6.7: Graph of the cross-correlation function of temperature data collected at 11 meters depth with respect to water level in the North Abandoned Well with 100 lags. On the x-axis is time in terms of lags (1 lag is equivalent to 10 minutes), and on the y-axis is the degree of cross-correlation.

The graphs of pH (Figure 6.8) and dissolved oxygen (Figure 6.9) with respect to time illustrate no temporal trends. The master correlogram (Figure 11.5) reveals significant correlations in the water level, specific conductance, and temperature data sets. Conversely, the correlation coefficients of pH and dissolved oxygen are 0 which indicated randomness. With respect to depth, the average pH increases from 7.10 at 7 meters to 7.37 at 11 meters (Figure 6.8). The average dissolved oxygen decreases from 4.65 mg/L at 7 meters to 2.58 mg/L at 11 meters. Conversely, the data set of dissolved oxygen (Figure 6.9) is dominated by a large perturbation to the system with a maximum value of 20.03 mg/L at 7 meters. This perturbation occurs 2 days after a significant rainfall event, and dissipated after approximately 3 days. Once equilibrium is reached the dissolved oxygen at both depths begin to converge.

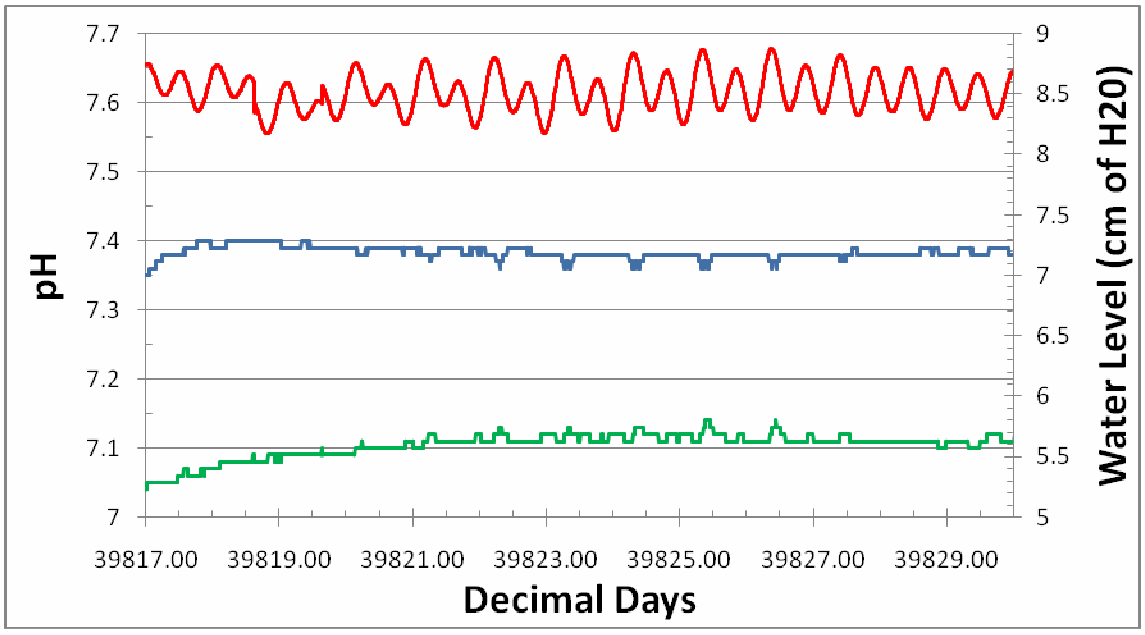

Figure 6.8: pH at depths of seven (green) and eleven (blue) meters are plotted on the primary vertical axis (left) with respect to time in decimal days. Water level data in cm of water (red) are plotted on the secondary vertical axis (right) with respect to time.

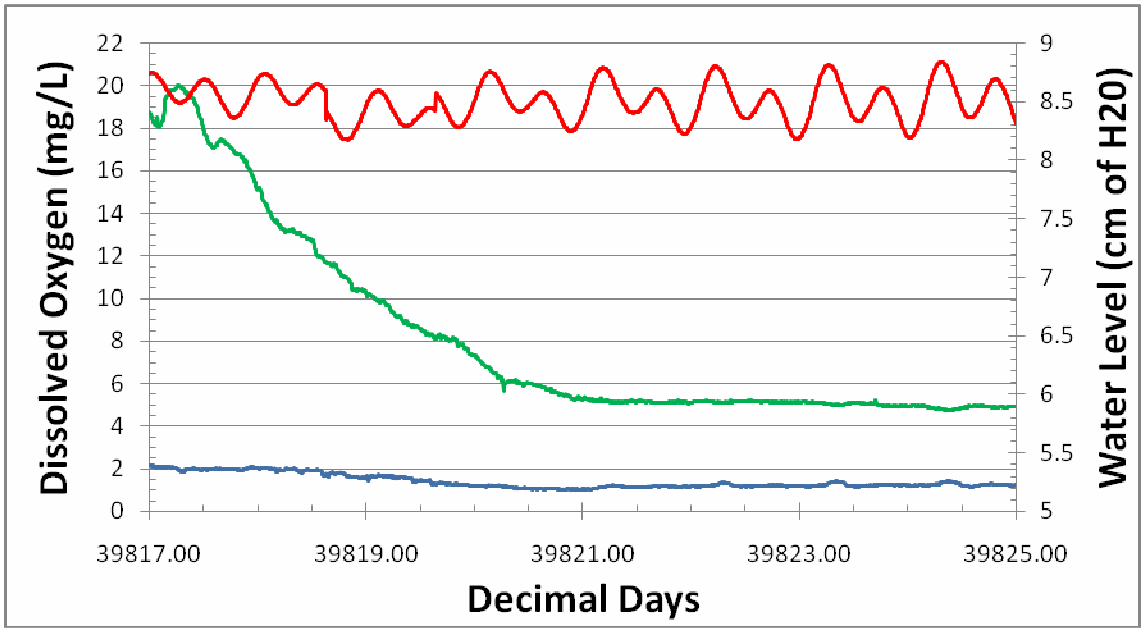

Figure 6.9: Dissolved Oxygen at depths of seven (green) and eleven (blue) meters are plotted on the primary vertical axis (left) with respect to time in decimal days. Water level data in cm of water (red) are plotted on the secondary vertical axis (right) with respect to time.

7. Electrical Resistivity Results

The subsurface cross section of the measured apparent resistivity at the beach transect is stratified to a depth of analysis of approximately 6.0 meters with zones of high resistivity (ρ_{app} > 2000 Ω·m) at 0 > z > -2.0 meters, followed by a zone of medium resistivity (ρ_{app} ~ 100 Ω·m) less than a meter thick, and a zone of lower resistivity (ρ_{app} ~ 10 Ω·m) at -2.0 > z > -6.0 meters. Below -6.0 meters the apparent resistivity distribution is mottled with resistivities ranging from approximately 50 to 0.04 Ω·m. The

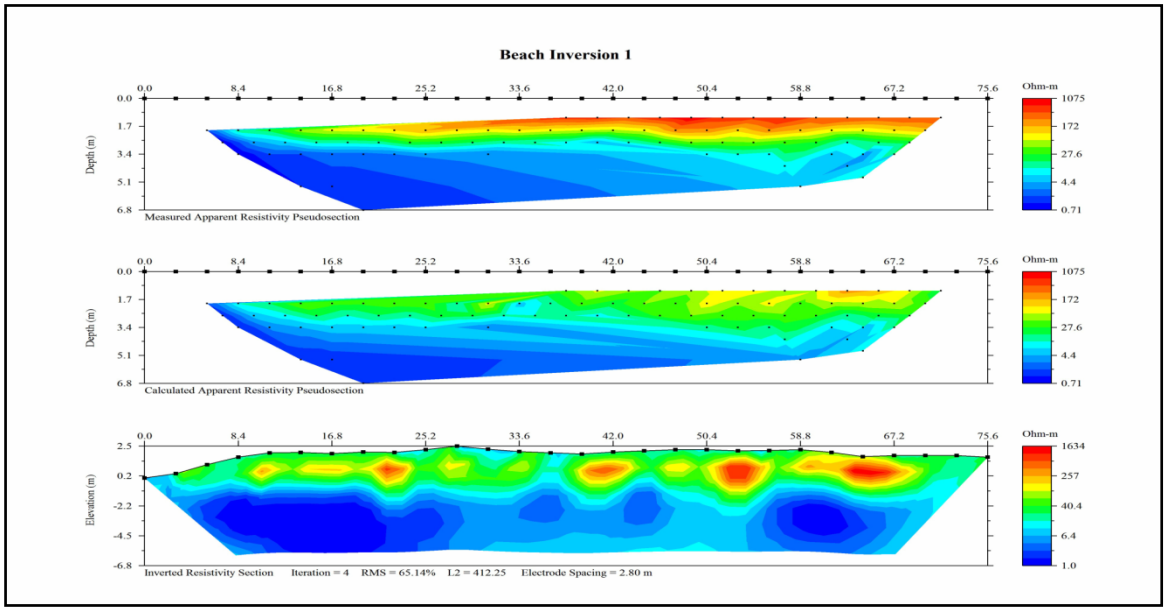

Figure 7.1: Electrical Resistivity Inversion model of the Beach transect generated using the Earth Imager 2D inversion software by Advanced Geosciences Inc. The Beach transect consists of 28 electrodes spaced 2.80 meters, and ends at the north edge of the road. The figure consists of three cross-sections: the first is a measured apparent resistivity pseudosection, the second is a calculated apparent resistivity pseudosection, and an inverted resistivity section. Electrical Resistivity in the 75.6 meter long model ranges from 1.0 to 1634 Ω·m, and has a maximum depth of penetration of 6.8 meters below sea level.

inversion

models of the electrical resistivity for the beach transect (Figure 7.1) has electrical resistivity values ranging from 1.0 to 1634 Ω·m, and has a maximum depth of penetration

of 6.8 meters below sea level. The model illustrates two separate zones of electrical resistivity with a transitional zone in between. Below a depth of 2 meters resistivity values do not exceed 6.4 Ω·m, and above 2 meters resistivity values range from 40.4 to 1634 Ω·m. This stratification is a relatively continuous feature that occurs from the swash zone at the beach across the Holocene strandplain. The model used 4 iterations, has an RMS of 65.14%, and an L2 of 412.25.

The subsurface cross section of the measured apparent resistivity at the ridge transect is stratified to a depth of approximately -6.0 meters with zones of resistivity on the order of 100 Ω·m that begins to pinch out at 30 meters horizontal distance. Below -6.0 meters the apparent resistivity distribution is mottled with resistivities ranging from

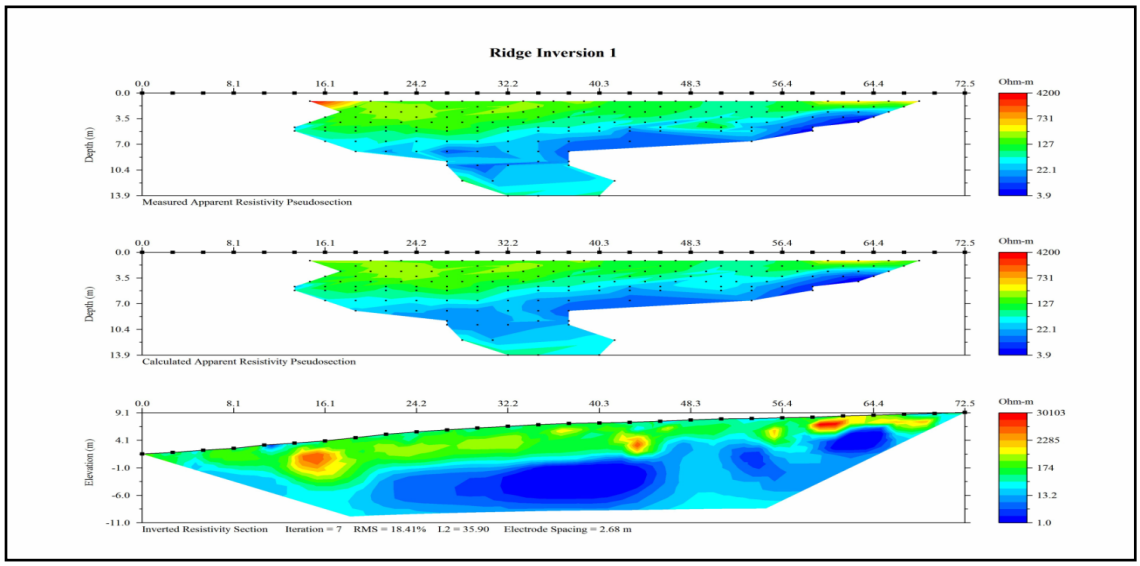

Figure 7.2: Electrical Resistivity Inversion model of the Ridge transect generated using the Earth Imager 2D inversion software by Advanced Geosciences Inc. The Ridge transect consists of 28 electrodes spaced 2.80 meters, begins at the south edge of the road and extend up the pleistocene ridge to approximately 5 meters north of the North 2 water well. The figure consists of three cross-sections: the first is a measured apparent resistivity pseudosection, the second is a calculated apparent resistivity pseudosection, and an inverted resistivity section. Electrical Resistivity in the 75.6 meter long model ranges from 1.0 to 30103 Ω·m, and has a maximum depth of penetration of 11.0 meters below sea level.

approximately 338 to 0.24 Ω·m. There is a large triangular anomaly, with $\rho_{app} >$ 100,000 Ω·m, from 0.0 to 18.0 meters horizontal distance that extends to a depth of approximately -5.0 meters. The inversion models of the electrical resistivity for the ridge transect (Figure 7.2) has electrical resistivity values ranging from 1.0 to 30,103 Ω·m, and has a maximum depth of penetration of 6.8 meters below sea level. The model illustrates two separate zones of electrical resistivity, and a transitional zone similar to the inversion model of the beach. Conversely, the upper-zone of high resistivity, which ranges from approximately 100 to 30103 Ω·m, is not laterally continuous like the Beach Inversion Model. The maximum depth of this high resistivity zone is approximately 6 meters below sea level and the minimum depth is 5 meters above sea level. The model used 7 iterations, has an RMS of 18.41%, and an L2 of 35.90.

The subsurface cross section of the measured apparent resistivity at the ridge transect is mottled throughout with a resistivity range of $0.08 < \rho_{app} <$ 10,000 Ω·m. There is a large triangular anomaly, with $\rho_{app} >$ 100,000 Ω·m, from 0.0 to 40.0 meters horizontal distance that extends to a depth of approximately -12.0 meters. The inversion models of the electrical resistivity for the long transect (Figure 6.4.3) has electrical resistivity values ranging from 6.0 to 64404 Ω·m, and has a maximum depth of penetration of 18.0 meters below sea level. The Long model illustrates a, irregular layering that mimics the Beach and Ridge models. Under most circumstances the high resistivity zone, which ranges from 65 to 64404 Ω·m, extends to depths similar to the Ridge model. The major difference in this model is the anomalously high resistivity zone from 0 to 25 meters along the transect. The model uses six iterations, has an RMS of 34.05, and a L2 of 123.53.

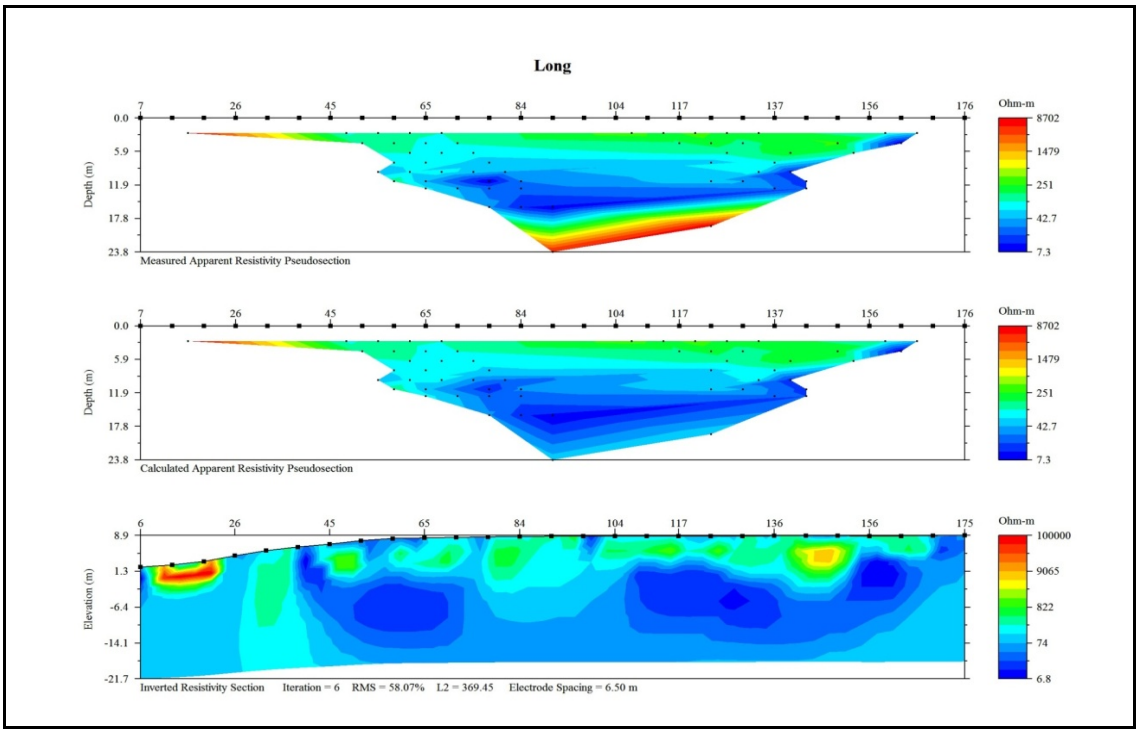

Figure 7.3: Electrical Resistivity Inversion model of the Long transect generated using the Earth Imager 2D inversion software by Advanced Geosciences Inc. The Long transect consists of 28 electrodes spaced 6.27 meters apart, begins at the south edge of the road and extend up the Pleistocene ridge to approximately 5 meters north of the North 2 water well. The figure consists of three cross-sections: the first is a measured apparent resistivity pseudosection, the second is a calculated apparent resistivity pseudosection, and an inverted resistivity section. Electrical Resistivity in the 168 meter long model ranges from 6.0 to 64404 Ω·m, and has a maximum depth of penetration of 18.0 meters below sea level.

8. Discussion

Using a combination of geochemical and geophysical methods the fresh water resources were studied in an abandoned well field on the northern shore of the island. The time-series analysis of water well geochemistry provides an understanding of the behavior of water resources with respect to time. Analysis of the distribution of the subsurface electrical resistivity was used to determine the dimensions of the fresh water lens and mixing zone. Due to the termination of pumping at the Line Hole well field it provides an excellent location to study the process of fresh water lenses restoration in eogenetic aquifers.

The primary temporal trend in Figure 6.1 is a mixed semi-diurnal cycle in water level. Conversely, spring and neap tides have much larger temporal scales than the daily tidal oscillations and therefore cannot be confirmed without a larger data set. The autocorrelation function for water level at 4000 and 100 lags (Figures 6.2 and 6.3) indicates that every 4.5 hours (27 lags) the water level in the well responds to a shift in the tides. Statistical analyses of specific conductance (Figures 6.4 and 6.5) and temperature also indicate the same temporal trend. The fresh water lens and its associated mixing zone are fixed geochemical zones within the phreatic zone. High tide causes a rise in water level, and this process causes the fresh water lens and mixing zone to be perched. The fixed geochemical datasondes record this movement of the fresh water lens and provide information on its temporal behavior. Analysis of water level with respect to precipitation (Figure 6.1) reveals that the effects of precipitation of fresh water lens morphology is negligible at small time scales. It can therefore be

hypothesized that low recharge rates and tidal forcing slows the growth of the fresh-water lens and promotes the development of a thick mixing zone. The dissolutionally-enhanced permeability of the Pleistocene bed rock allows for the high tidal communication in the Line Hole well field. The lack of wells in Holocene sediment and beach rock prevent any temporal analysis of the water chemistry. Conversely, it is hypothesized that the lower permeability of the Holocene deposits with respect to the Pleistocene bed rock would limit tidal forcing, and promotes a thicker fresh-water lens.

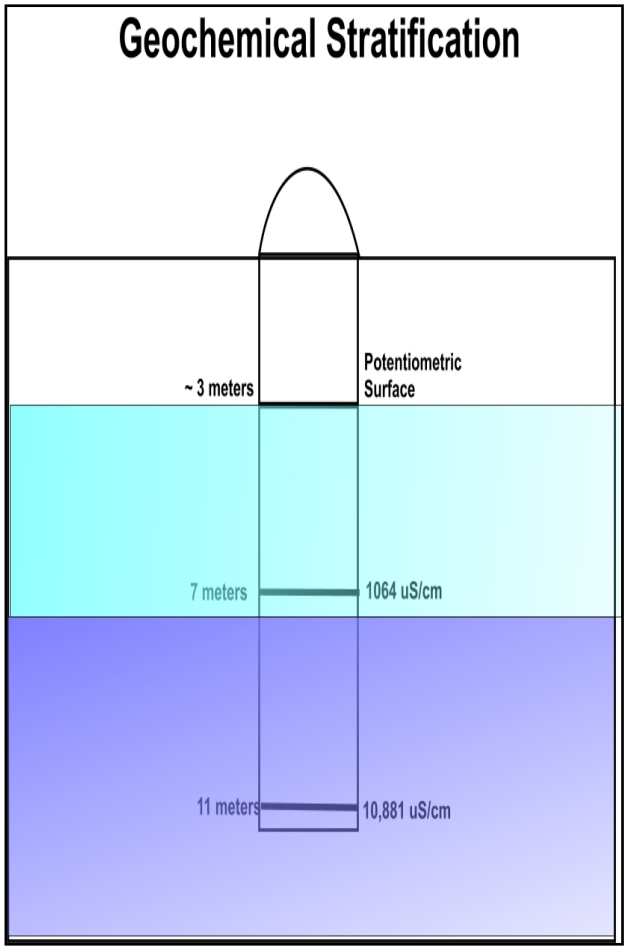

Figure 8.1: Diagram of the geochemical stratification in the north abandoned water well. The thresholds illustrated in the diagram are approximated according to Figure 6.4, and is not to scale. The potentiometric surface is at an average depth and the depth of the geochemical datasondes (7 and 11 meters) is used to approximate the thickness of the potentiometric surface. The light blue zone on the diagram is indicative of fresh water, and the dark blue is brackish water.

The Ghyben-Herzberg Principle describes the morphology of fresh-water lenses, and geochemical stratification of water in coastal aquifers. Time-series specific conductance data collected at depths of 7 and 11 meters (Figure 6.4) illustrates an increase in specific conductance with depth. Russell and Kane (2005) set the following intervals for specific conductance: 0-1,300 µS/cm for fresh water, 1,301-28,800 µS/cm for brackish water, and specific conductance greater than 28,801 µS/cm is considered saline. Average specific conductance at 7 meters depth

is 1064 µS/cm, and at 11 meters depth is 10,881 µS/cm. Using the classification system of Russell and Kane (2005); the water at 7 meters depth is considered fresh, but is bordering on brackish. The water at 11 meters depth is considered brackish, and is approximately midway between fresh and saline. Using the measured potentiometric surface depth of approximately 3 meters; the fresh water lens is approximately 4 meters thick according to the specific conductance dataset (Figure 8.1). The final 4 meters of investigation are all in the mixing zone, and it can be assumed that the mixing zone extends several meters below the bottom of the well.

The stratification of pH is described by Figure 6.1.5 which illustrates an increase in pH with respect to depth. The density contrast of the potentiometric surface results in an accumulation of organic matter, and bacteria (Schwabe, 1999; Schwabe, 2002). It can therefore be hypothesized that the decay of organic matter, bacterial respiration, and acidic rainfall lowers the pH near the top of the potentiometric surface. These processes are important in lowering pH because various researchers feel that CO_2-degassing raises pH at the potentiometric surface (Schwabe, 1999; Schwabe, 2002). Conversely, extensive buffering of the solution from the limestone bedrock, and possibly addition of basic marine water via salt water intrusion are the most likely causes of the pH increase with respect to depth.

Time-series analysis of dissolved oxygen (Figure 7.1.7) illustrates an increase in dissolved oxygen with depth. Conversely, there is a reversal of this trend on January 18, 2009 and the 11-meter datasonde begins recording higher dissolved oxygen than the 7 meter datasonde. These differences in dissolved oxygen with respect to depth can be attributed to interactions with the atmosphere, decaying organic matter, and possibly salt

water intrusion. In general, shallow water has higher concentrations of dissolved oxygen due to interactions with the oxygen-rich atmosphere. Conversely, the decay of organic matter at the top of the potentiometric surface can create anoxic conditions (Schwabe, 1999; Schwabe 2002). The balance between these two processes determines the dissolved oxygen gradient in the phreatic zone. The increase in dissolved oxygen with respect to depth indicates that uptake of atmospheric oxygen is overwhelming the effects of the decay of organic matter. The reversal of this gradient can most likely be attributed to an increase in organic matter at the top of the potentiometric surface. Salt water intrusion supplying oxygenated marine waters to the bottom of the mixing zone may also be playing a role in this reversal.

Time-series temperature collected at depths of 7 and 11 meters (Figure 7.1.8 and 7.1.9) illustrates an increase in temperature with depth. These differences in temperature with respect to depth can be attributed to interactions with the atmosphere, and salt-water intrusion. In general, water at or near the potentiometric surface receives more solar radiation than deeper water. This process sufficiently explains the decrease in temperature with respect to depth. Conversely, as air temperatures increase in the summer months; the water temperature in the lagoons and inland lakes increases. This process has the potential to reverse the depth profile of temperature. Tidal forcing of warm lagoon and lake water into the aquifer can create warmer temperatures deeper in the subsurface.

The model of the electrical resistivity distribution of the beach transect (Figure 6.4.1) illustrates two separate zones of electrical resistivity with a transitional zones. This layered resistivity distribution is a relatively continuous feature that occurs from the

swash zone at the beach to the end of the transect. Using common electrical resistivity values (Figure 4.2.1) there appears to an approximately 1 meter thick vadose zone with a resistivity signature over 1,000 Ω·m. The area below this 1 meter thick vadose zone has a resistivity signature ranging from 100 to 1 Ω·m. This signature is indicative of various degrees of brackish water throughout the rest of the profile. The presence of the Holocene/Pleistocene lithological contact is not evident in the model, but appears in the raw apparent resistivity measurements. The lack of a lithological contact is most likely due to edge effects in the inversion models due to the position of the anomaly under the first 6 electrodes. The Holocene dune ridge and strandplain are underlain by a thin lens of drinkable water, and a much thicker, diffuse transition zone to a depth of at least 6.8 meters. These high error values indicate a high degree of noise in the data. This can be attributed to the age of the equipment used and the high conductivity of the subsurface. The relatively high porosity and permeability of the eogenetic limestones allow for large volumes of water to be held within the rock. The amount of current induced by the Sting R1 Earth Resistivity is not high enough to effectively resolve finer differences in the subsurface resistance. Newer versions of this equipment induce a much larger current into the subsurface, and therefore amplify the contrast between materials.

The model of the electrical resistivity distribution of the ridge transect (Figure 6.4.2) illustrates two separate zones of electrical resistivity with transitional zones associated, similar to the inversion model of the beach transect. Conversely, the upper-zone of high resistivity, which ranges from approximately 100 to 30103 Ω·m, and is not laterally continuous like the inversion model of the beach transect. The maximum depth of this high resistivity zone is approximately 6 meters below sea level and the minimum

depth is 5 meters above sea level. Modeled resistivity values that exceed 1,000 Ω·m are indicative of a vadose zone. Using the occurrence of these high resistivity models allows us to approximate that the vadose zone in this area extends from a depth of 2 meters below the surface at the beginning of the profile, and to a depth of 1 meter below the surface at the top of the Pleistocene dune ridge. The thickness of this vadose zone ranges from 1 to 2 meters depending on the position along the profile. The phreatic zone is associated with resistivities ranging from 1 to 100 Ω·m. The thickest zone of fresh water occurs at the beginning of the transect presumably due to the presence of a lithological contact between Holocene and Pleistocene rocks. This feature is not illustrated in the model, but is observable in the measured pseudosection. The Holocene sands act as a hydrological barrier which causes the fresh water to accumulate along this contact (Vacher, 1988). Despite the high accuracy relative to the other profiles; the noise generated by the conductive subsurface still causes an undesirable amount of error.

The model of the electrical resistivity distribution of the long transect (Figure 6.4.3) illustrates two separate zones of electrical resistivity with transitional zones associated, similar to the inversion model of the beach transect. Under most circumstances the high resistivity zone, which ranges from 65 to 64,404 Ω·m, extends to depths similar to the Ridge model. The depths of the hypothesized fresh water lens and mixing zone in this model correspond to the moderately well with the geochemical data from the north abandoned water well. The basal contact of the mixing zone is not evident in the model presumably due to the lack of resolution with depth inherent in the dipole-dipole array. Along with the stratified electrical resistivity distribution the long model has an anomalously high resistivity zone from 0 to 25 meters along the transect. This

feature can either be explained by effects of the Holocene/Pleistocene lithological contact, or error in the model.

Both datasets provide meaningful information on the behavior and morphology of the fresh water lens at the Line Hole well field. The geochemical data reveal tidal influences on fresh water lens position, and provide a one-dimensional profile of geochemical chemical stratification at the north abandoned water well. The analysis of geochemical is short-term and only spans part of the dry season. It is therefore difficult to gain an accurate understanding of the fresh water resources on the island without a larger dataset. The inversion models of electrical resistivity, which are believed to be the most definitive method of imaging the fresh water lens and mixing zone, lack accuracy due to the high levels of noise. In terms of the accuracy of this method the equipment being used is a large factor. Since it is often difficult to accurately delineate the potentiometric surfaces, further analysis of these models can be misleading. Despite these pitfalls, the extent of the fresh-water lens and transition zone can be approximated using this method. When these models are cross-referenced to the geochemical analyses there is agreement on the dimensions of the fresh water lens on the Pleistocene dune ridge. Both datasets indicate a thin lens of fresh drinking water that is underlain by a thick, diffuse zone of mixing. Unfortunately, without wells in the Holocene strandplain it is impossible to accurately cross-reference the geochemical data with the inversion model of the beach transect. Despite the errors identified above; the results gathered in this case study indicate that this method has the potential to be effective in this setting. If the error of the inversion models can be decreased then there can be more confidence in the interpretations of the extent of fresh water lens.

9. Conclusions

Geochemical and electrical resistivity data collected at the Line Hole well field from January 1 to June 29, 2009 are used to describe the extent and behavior of fresh water resources on San Salvador Island. The following conclusions were derived using this data set. (1) The North Abandoned water well is connected through preferred flow pathways to the ocean. This connection is evident by the mixed semi-diurnal signal in the water level data for the water well. (2) The over-pumping that culminated in December, 2006 has caused severe depletion of the fresh water lens that still exists today. The mixing zone of the fresh water lens at the North Abandoned water well in the Line Hole well field exceeds 4 meters in thickness, and at times is thicker than the fresh water lens. (3) Noise generated from the highly conductive subsurface creates high levels of error, and makes the effectiveness of this method undesirable. Conversely, more updated equipment with a capacity to induce a larger current in the subsurface can limit the noise, and therefore limit the error. (4) Finally, despite the noisy electrical resistivity data the size and extent of the fresh water lens, and mixing zone underlying the Line Hole well field can be approximated.

The geology of San Salvador Island is diverse, and it is suspected that the geology plays a large role on the location and extent of fresh water. The relationship between tidal-forcing and well water chemistry may not be as robust in other areas of the island. Specifically locations underlain by low permeability, high porosity Holocene units may respond very different to this process. To gain a more complete assessment of the fresh

water resources on San Salvador Island, other areas of the island need to be studied. This provides the ability to compare and contrast the fresh water lens at different locations which can guide a more accurate model for the island as a whole.

10. References

Back, W., Hanshaw, B.B., Herman, J.S., and Van Driel, J.N., 1986, Differential dissolution of a Pleistocene reef in the ground water mixing zone of coastal Yucatan, Mexico: Geology, v. 14, -. 137-140.

Back, W., 1988, Region 26, West Indies, The Geology of North America, Hydrogeology, v. O-2, p.

Budd D.A., Saller A.H. and Harris P.A. (Eds), 1995. Unconformities in Carbonate Strata – Their Recognition and the Significance of Associated Porosity, AAPG Memoir 63, 55-76.

Budd, D. A., Vacher, H. L., 2004, Matrix Permeability of the Confined Floridan Aquifer, Florida, USA, Hydrogeology Journal, v. 12, p. 531- 549.

Cant, R.V., 1996, Water supply and sewage treatment in a small island environment: the Bahamian experience. In Maul, G.A., ed., Small islands: marine science and sustainable development, p. 329-340. Washington D.C.: American Geophysical Union.

Crump, M.A., and Gamble, D.W., 2006, Hydroclimatic analysis of a carbonate island pond through the development of a hydrologic landscape unit model, Physical Geography, v.27, 6, p. 554-570.

Davis, R. L., and Johnson, Jr., C.R., 1989, Karst hydrology of San Salvador, in Curran, H.A., ed., Proceedings of the Third Symposium on the Geology of the Bahamas: San Salvador, Bahamian Field Station, p. 118-136.

Erdman, J.S., Key, Jr. M. M, and Davis, R.L., 1997, Hydrogeology of the Cockburn Town Aquifer, San Salvador Island, Bahamas, and the change in water quality resulting from the development of a resort community, in Curran, H.A., ed., Proceedings of the Eighth Symposium on the Geology of the Bahamas and Other Carbonate Regions: Bahamian Field Station, San Salvador. Pp. 47-58.

Gamble, D.W., M.E. Brown, D. Parnell*, D. Brommer*, and P.G. Dixon*, 2000. Lessons learned from field evaluation of Hurricane Floyd damage on San Salvador Island, Bahamas. *Bahamas Journal of Science*, 8(1): 25-31.

Gaughan, M., and Davis, R.L., 2009, Water Quality changes in a karst aquifer following abandonment of a well field: Line Hole, San Salvador Island, Bahamas. Geological Society of America *Abstracts with Programs*, Vol. 41, No. 7, p. 466

Ghyben, H. W., 1888, Nota in verbandmet de voorgenomen putoboring nabij Amsterdam. Tijdschrift van Let Koniklijk Instituut can Ingenieurs, The Hague, Netherlands, p. 8-22.

Herzberg, A., 1901, Die Wasserversorgung einiger Nordseebader, Wasserversorgung, v. 44, p. 815-819 and 842-844.

Klein, H., Hoy, N.D., and Sherwood, C.B., 1958, Geology and groundwater resources in the vicinity of the auxiliary Air Force bases, British West Indies: United States Department of the Interior, Geological Survey, 150 p.

Kunze, A.W.G, and Quick, T.J., 1994, Tidal water- level fluctuations in water wells on San Salvador Island, Bahamas: American Association of Engineering Geologists, v. 31, p. 75-89.

Little et al., 1977, Land Resources of the commonwealth of the Bahamas, 4, Andros Island, Unpublished report for the Ministry of Overseas Development, Surbiton, England, 198 pages.

Meyerhoff, A. A., and Hatten, C. W., 1974, Bahamas Salient of North America: Tectonic Framework, Stratigraphy, and Petroleum Potential, American Association of Petroleum Geologists Bulletin, v. 58, p. 1201-1239.

Mylroie, J.E., Carew, J. L, 2008, Field Guide to Geology and Karst Hydrogeology of San Salvador Island. Bahamian Field Station, San Salvador Island, Bahamas

Mylroie, J. E., Carew, J. L., and Vacher, H. L., 1995, Karst Development in the Bahamas and Bermuda, Geological Society of America Special Paper 300.

Roebuck, L., Pochatila, J., and Ortiz, T., 2004, Water Resource Assessment of the Bahamas, US Army Corps of Engineers, Mobile District & Topographic Engineering Center.

Russell, G.M., and Kane, R.L., 2005. Bathymetry, Freshwater Flow, and Specific Conductance of Matlacha Pass, Southwestern Florida, Water Resources Investigations Report 93-4057, U.S. Department of the Interior, U.S. Geological Survey.

Schneider, J.A. and S.E. Kruse, Assessing natural and anthropogenic impacts on freshwater lens morphology on small barrier islands: Dog Island and St. George Island, Florida, *Hydrogeology Journal*, 14, 131-145, doi 10.1007/s10040-005-0442-9, 2005.

Schwabe, S.J., 1999, Biogeochemical investigation of submerged caves within Bahamian carbonate platforms, Ph. D. thesis, University of Bristol, UK, 235 p.

Schwabe, S.J., 2002, Biogeochemical processes that influence cave development within Bahamian carbonate platforms, *In* Martin, J.B., Wicks, C.M., and Sasowsky, I.D. eds., Proceedings of the Symposium Karst Frontiers: Florida and Related Environments: Karst Waters Institute Special Publication 7, p. 103-106.

Sealey, 1994, Bahamian Landscapes: An introduction to the Geography of the Bahamas (Second Edition), Nassau, Bahamas: Media Publishing.

Shaklee, R.V., 1996, Weather and climate of San Salvador Island. San Salvador, Bahamas: Bahamian Field Station.

Smart et al., 2006, Cave Development on the Caribbean Coast of the Yucatan Peninsula, Quintana Roo, Mexico, Perspectives on Karst Geomorphology, Hydrology and Geochemistry, Geological Society of America Special Paper 404, p. 105-128.

Whitaker, F. F., Smart, P. L., 2004, Hydrogeology of the Bahamian Archipelago, Geology and Hydrogeology of Carbonate Islands, Elsevier, ch.4, p. 183-216.

Vacher, H. L., 2004, Introduction: Varieties of Carbonate Islands and a Historical Perspective, Geology and Hydrogeology of Carbonate Islands: Developments in Sedimentology, Elsevier, ch. 1, p. 1-34.

Vacher, H.L., 1988, Dupuit-Ghyben-Herzberg analysis of strip island lenses: Geological Society of America Bulletin, v.100, p. 580- 591.

11. Appendix

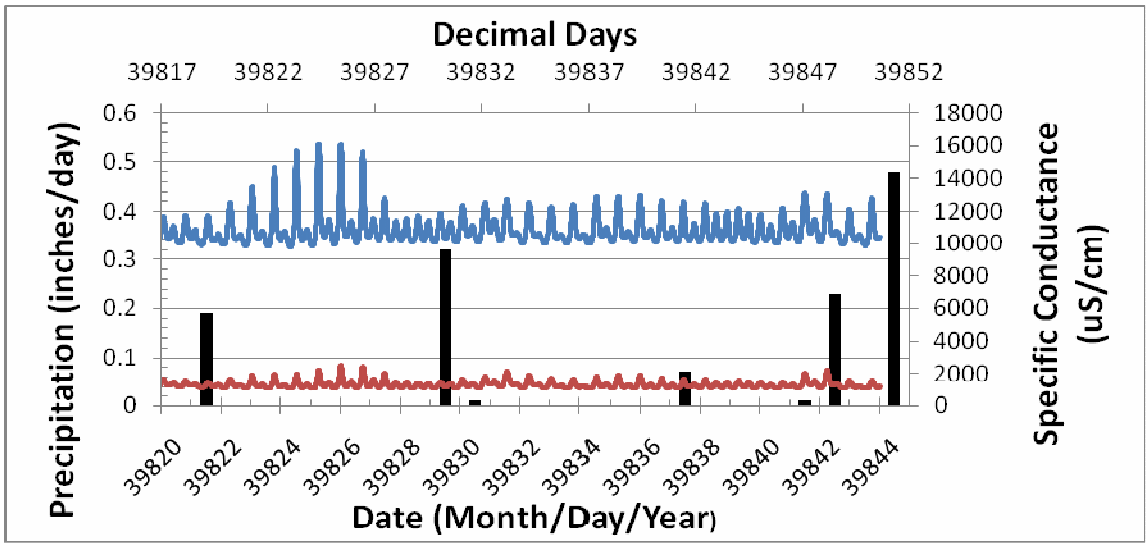

Figure 11.1: Time-series graph of precipitation and specific conductance with respect to time. On the primary y-axis is precipitation (black) measured in inches per day, and on the primary x-axis is the date of rainfall events. On the secondary y-axis is specific conductance in µS/cm, and on the secondary x-axis is time measured in decimal days. Specific conductance is being plotted for each datasonde: the shallow datasonde was placed at a level of 7 meter, and the deep datasonde was placed at a depth of 11 meters.

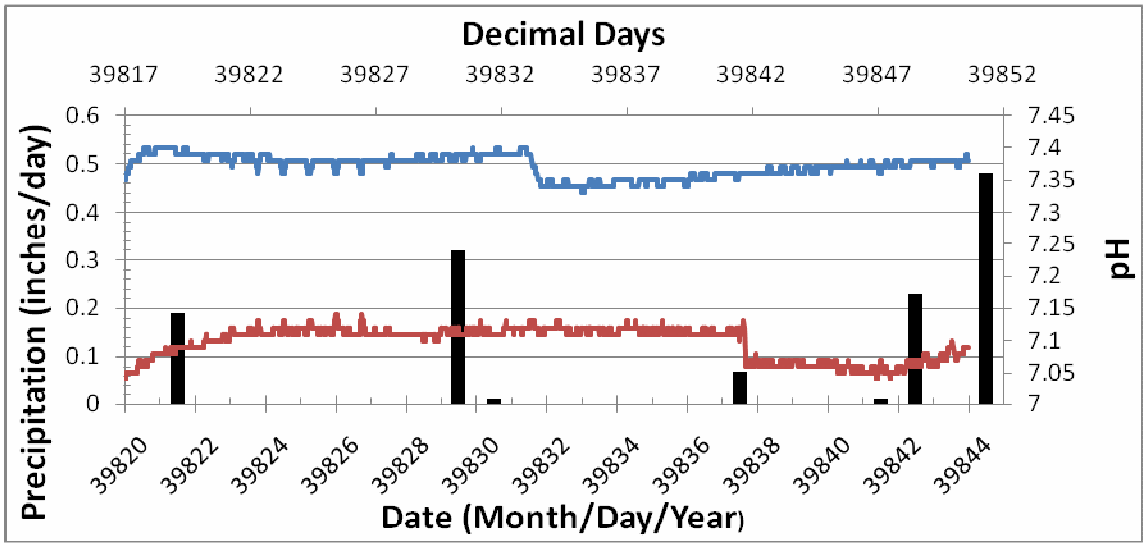

Figure 11.2: Time-series graph of precipitation and pH with respect to time. On the primary y-axis is precipitation (black) measured in inches per day, and on the primary x-axis is the date of rainfall events. On the secondary y-axis is pH, and on the secondary x-axis is time measured in decimal days. pH is being plotted for each datasonde: the shallow datasonde was placed at a level of 7 meter, and the deep datasonde was placed at a depth of 11 meters.

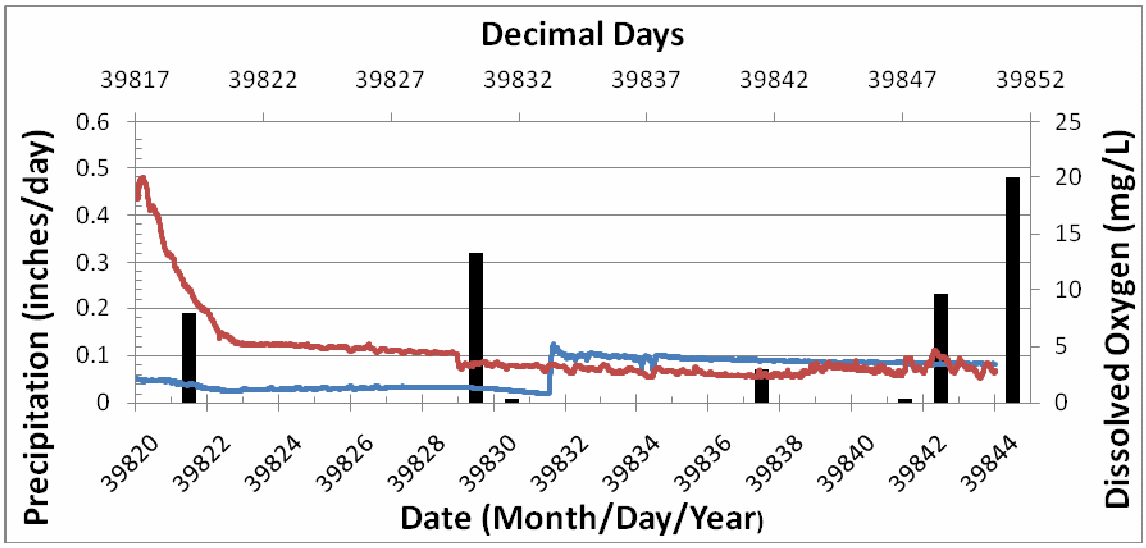

Figure 11.3: Time-series graph of precipitation and Dissolved Oxygen with respect to time. On the primary y-axis is precipitation (black) measured in inches per day, and on the primary x-axis is the date of rainfall events. On the secondary y-axis is dissolved oxygen, and on the secondary x-axis is time measured in decimal days. Dissolved oxygen is being plotted for each datasonde: the first datasonde was placed at a level of 7 meter (red), and the second datasonde was placed at a depth of 11 meters (blue).

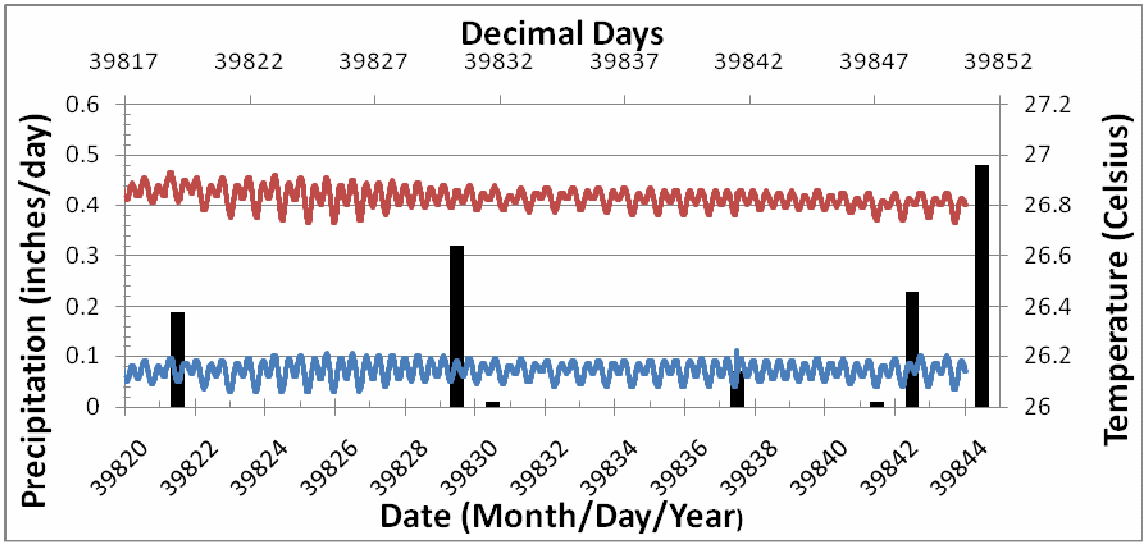

Figure 11.4: Time-series graph of precipitation and Dissolved Oxygen with respect to time. On the primary y-axis is precipitation (black) measured in inches per day, and on the primary x-axis is the date of rainfall events. On the secondary y-axis is dissolved oxygen, and on the secondary x-axis is time measured in decimal days. Dissolved oxygen is being plotted for each datasonde: the first datasonde was placed at a level of 7 meter (red), and the second datasonde was placed at a depth of 11 meters (blue).

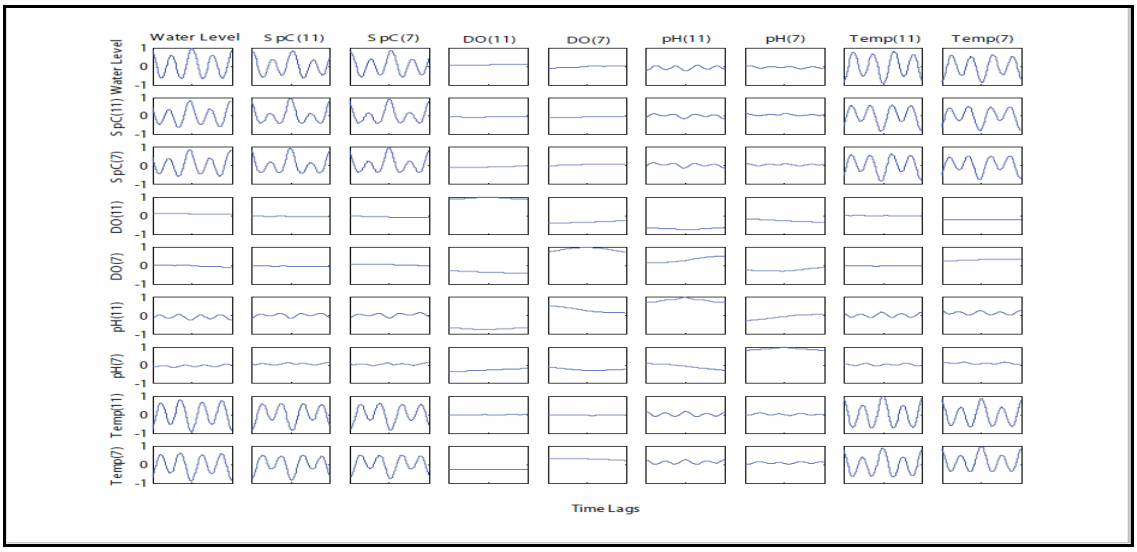

Figure 11.5: Autocorrelation and crosscorrelation functions of all geochemical variables collected at the Line Hole well field (water level at 10 meters, specific conductance at 11 and 7 meters, pH at 11 and 7 meters, dissolved oxygen at 11 and 7 meters, and temperature at 11 and 7 meters) plotted as a function of time lags. Time lags (1 lag corresponds to a 10 minute shift in time) is plotted on the x-axes of all sub-plots, and the correlation coefficient from -1 (negative correlation) to 1 (positive correlation) is plotted on the y-axes of all sub-plots.

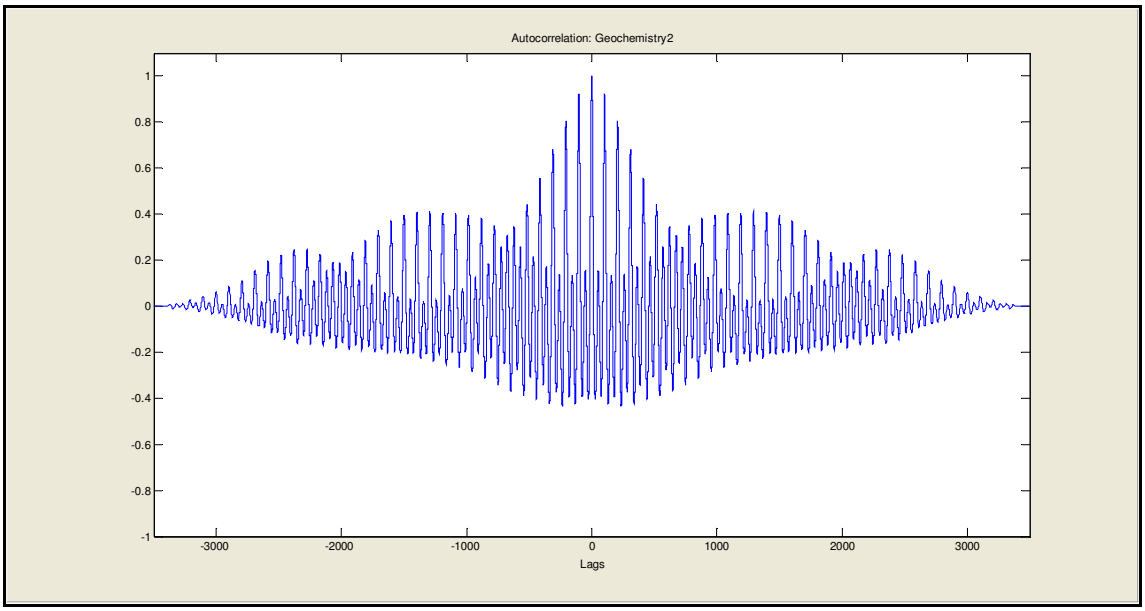

Figure 11.6: Graph of the autocorrelation function of specific conductance data collected at 11 meters depths in the North Abandoned Well with 4000 lags. On the x-axis is time in terms of lags (1 lag is equivalent to 10 minutes), and on the y-axis is the degree of autocorrelation.

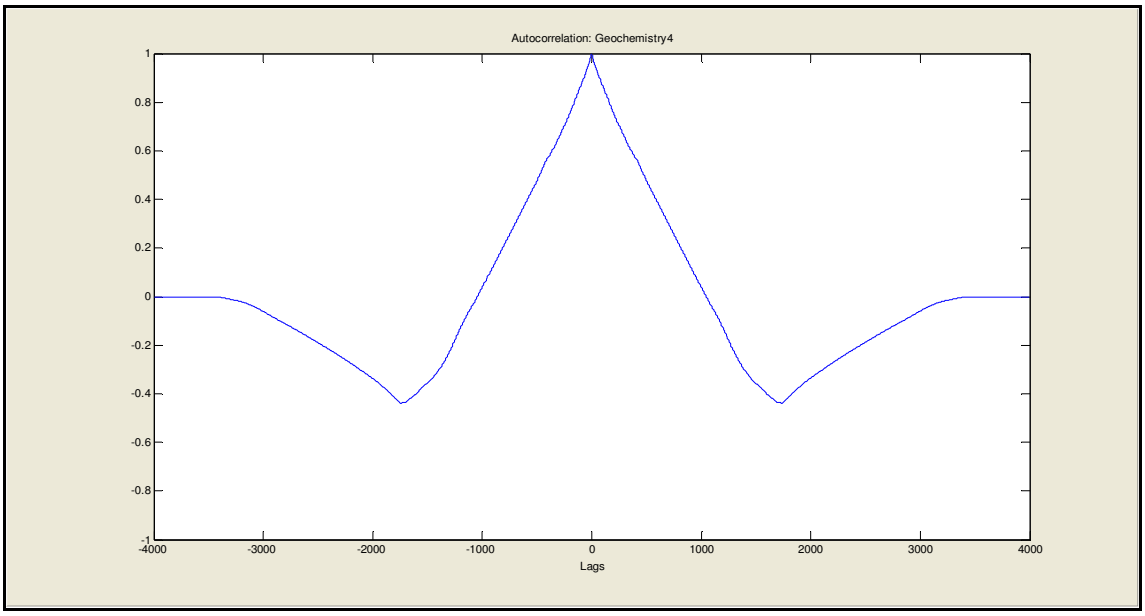

Figure 11.7: Graph of the autocorrelation function of dissolved oxygen data collected at 11 meters depths in the North Abandoned Well with 4000 lags. On the x-axis is time in terms of lags (1 lag is equivalent to 10 minutes), and on the y-axis is the degree of autocorrelation.

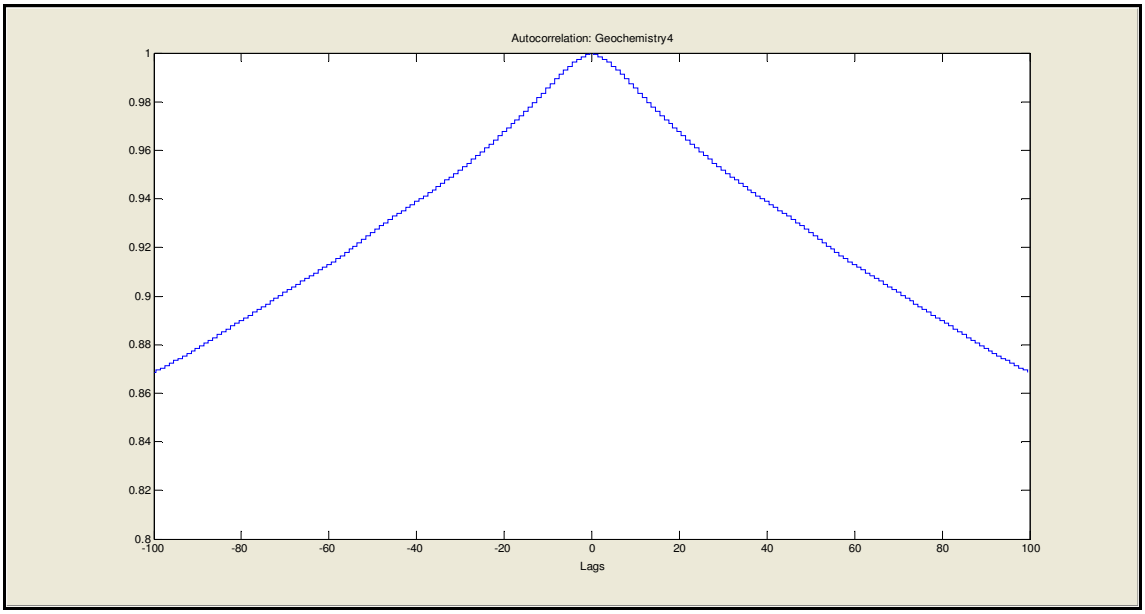

Figure 11.8: Graph of the autocorrelation function of dissolved oxygen data collected at 11 meters depths in the North Abandoned Well with 100 lags. On the x-axis is time in terms of lags (1 lag is equivalent to 10 minutes), and on the y-axis is the degree of autocorrelation.

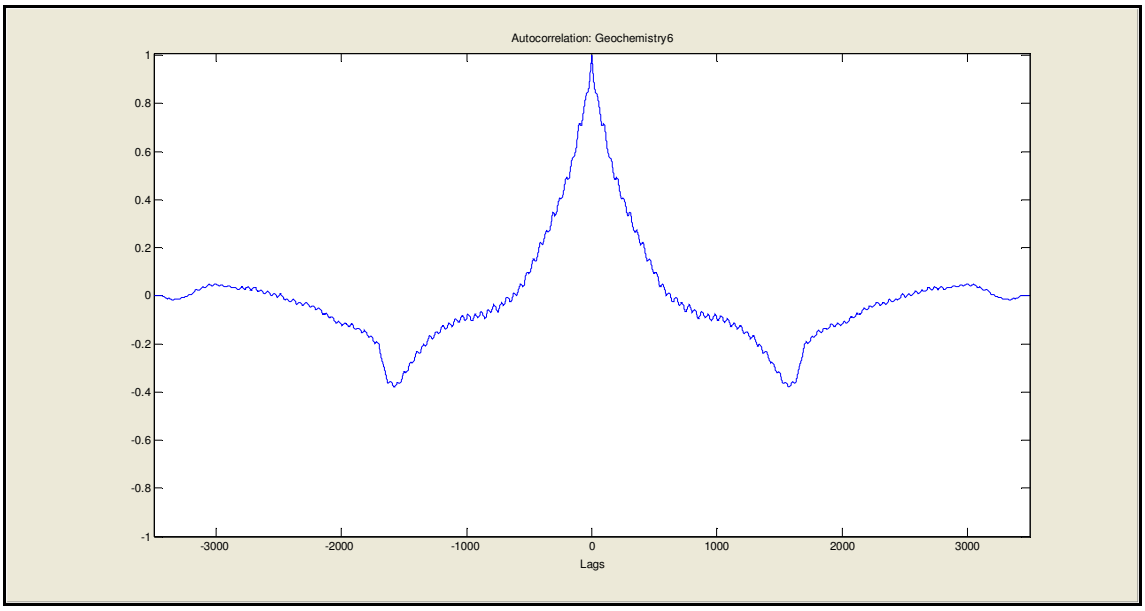

Figure 11.9: Graph of the autocorrelation function of pH data collected at 11 meters depths in the North Abandoned Well with 4000 lags. On the x-axis is time in terms of lags (1 lag is equivalent to 10 minutes), and on the y-axis is the degree of autocorrelation.

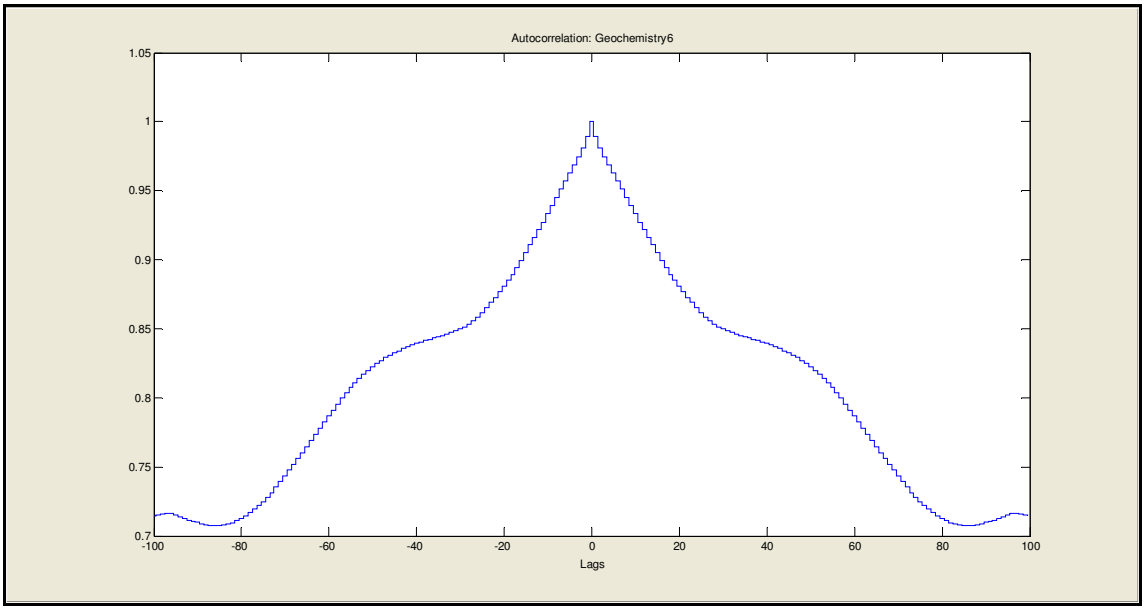

Figure 11.10: Graph of the autocorrelation function of pH data collected at 11 meters depths in the North Abandoned Well with 100 lags. On the x-axis is time in terms of lags (1 lag is equivalent to 10 minutes), and on the y-axis is the degree of autocorrelation.

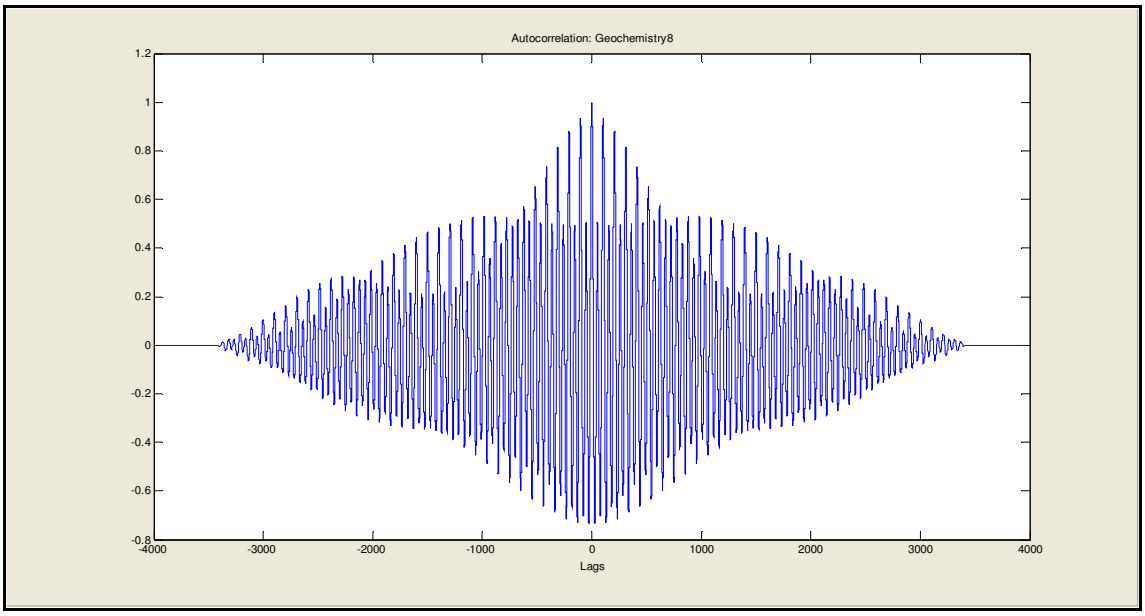

Figure 11.11: Graph of the autocorrelation function of temperature data collected at 11 meters depths in the North Abandoned Well with 4000 lags. On the x-axis is time in terms of lags (1 lag is equivalent to 10 minutes), and on the y-axis is the degree of autocorrelation.

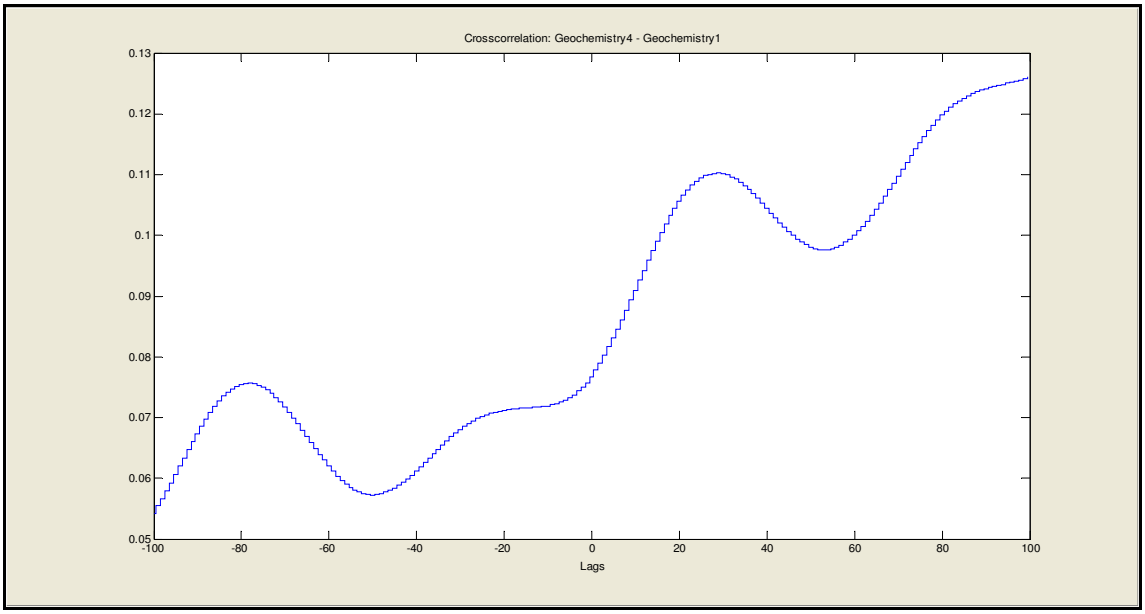

Figure 11.12: Graph of the cross-correlation function of dissolved oxygen with respect to water level data collected at 11 meters depths in the North Abandoned Well with 100 lags. On the x-axis is time in terms of lags (1 lag is equivalent to 10 minutes), and on the y-axis is the degree of autocorrelation.

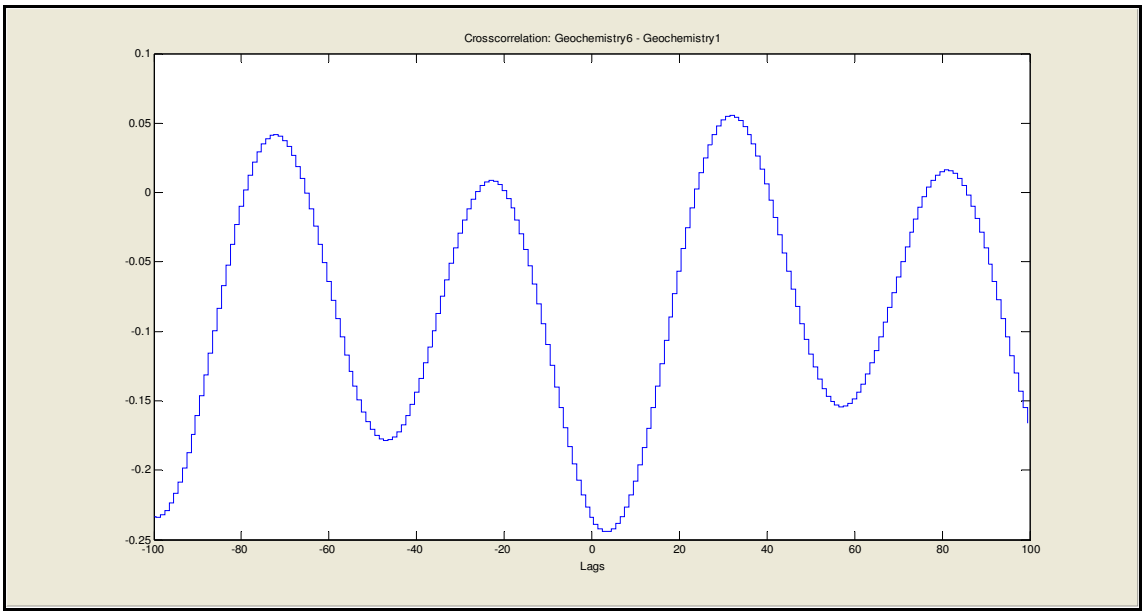

Figure 11.13: Graph of the cross-correlation function of pH with respect to water level data collected at 11 meters depths in the North Abandoned Well with 100 lags. On the x-axis is time in terms of lags (1 lag is equivalent to 10 minutes), and on the y-axis is the degree of autocorrelation.